

**Warsaw University
Faculty of Physics**

Mateusz Kapusta

Index number: 431289

Search for dormant Black Holes in the OGLE data.

Bachelor degree in the field of Astronomy

Thesis written under supervision of
dr Przemysław Mróz
Astronomical Observatory
Warsaw University

Warsaw, May 2023

Abstract

In the work analysis of light curves from OGLE data was performed with goal to look for objects with possible black hole companions based on the ellipsoidal modulation of light curves. Each object is examined using Spectral Energy Density fits allowing to distinguish between stars composed from two objects with different temperature and single objects. Selection process resulted in 14 potential objects out of which one turned out to be spotted star while rest are considered as black hole binaries candidates. Detailed analysis of the objects is conducted estimating basic parameters of objects like temperature, mass, radius and in some cases estimate of radial velocity. Although at the end alternative explanation for ellipsoidal modulation is given no conclusion is reached as objects should be further investigated using spectroscopic observation in order to accept or reject hypothesis about compact companions.

Keywords

Dormant Black Holes,

Thesis title in Polish language

Poszukiwanie uśpionych czarnych dziur w danych z przeglądu OGLE.

Contents

1. Introduction	3
2. Theoretical considerations	6
2.1. Morris & Naftilan expression	6
2.2. Amplitude correction	7
2.3. Limitations	8
2.4. Modified mass ratio	8
2.5. Selection process	9
3. Observational data	10
3.1. Description of data and preprocessing	10
3.2. Spectral Energy Distribution	13
4. Results	18
4.1. Physical parameters of objects	18
4.2. Radial velocity semi-amplitude estimation from Gaia DR3 data	19
4.3. Detailed analysis of objects	20
4.3.1. GD1070.18.22288	21
4.3.2. SMC720.28.40576	24
4.3.3. Rest of objects	26
5. Discussion	29
Bibliography	30
Appendices	34
A. Spectral Energy Distribution plots	36
B. Semi-amplitude estimate from Gaia DR3	50

Chapter 1

Introduction

According to current knowledge most of the massive stars end their evolution as black holes, further investigation suggest existence of $\mathcal{O}(10^8)$ stellar mass BH's (Brown & Bethe, 1994) in our galaxy. Despite huge theoretical expectations only few tens of such objects have been found up to day. Since the discovery of first black hole binary Cygnus X-1 many researchers tried to tackle the problem employing numerous methods with particular success achieved in the field of X-ray based observations.

X-ray emitting objects can be roughly grouped into two categories: low mass X-ray binaries and high mass X-ray binaries (referred to as LMXB and HMXB). Low mass binaries are composed of compact object that is accreting matter from low mass companion overflowing it's Roche lobe. On the other hand high mass X-ray binaries accrete matter from stellar wind that is being created by high mass companion star. X-ray emission from X-ray binaries is mostly transient in character (Belloni & Motta, 2016) due to the accretion disc instabilities (Lasota, 2001). Many of X-ray binaries can remain undetected in low accreting regime for long periods, in order to find such objects all-sky monitoring in X-ray is necessary. According to Corral-Santana et al. (2016) only 64 stellar BH X-ray binaries have been detected up to date while only 5 of them are considered to be persistent sources.

In recent years new stellar mass BH's candidates are being found due to the new methods not based on X-ray emission. New generations of sky survey including spectroscopic surveys like APOGEE, LAMOST and GALAH can provide radial velocity information for millions of stars. Such information itself can be used to search for the compact objects and there are numerous candidates for compact binaries that are dormant in X-ray including black hole binaries (Liu et al., (2019), Jayasinghe et al., (2019), Shenar et al., (2022), Lennon et al. (2022), Thompson et al., (2019)). Although many of those claims have been disputed one can expect such surveys to provide increasing number of potential black hole binaries. Unfortunately even wide field multi-fiber spectroscopic devices cannot observe as many objects at once as wide field photometric devices limiting size of the sample that can be studied with such type of survey. There are also new discoveries of potential black hole binaries using Gaia astrometric observations paried with spectroscopic follow-up observations (El-Badry et al., (2022),ref). This

type of observations is available only for relatively small sample of objects (~ 30000) at the moment but with next releases of Gaia data potential this number is expected to rise significantly. Binaries with sufficiently long periods paired with low parallaxes allow to resolve components of binaries and trace apparent movement of the components on the sky. Compared to X-ray observations astrometric measurements allow to estimate parameters of the objects with much better accuracy as they allow to infer inclination of binary. This crucial parameter is very hard to constrain, it's usually estimated by modeling ellipsoidal effect visible in the light curve which can be lead to mass overestimation as demonstrated by (Kreidberg et al., 2012).

Third kind of observations allowing to search for black holes that already led to the discovery of isolated stellar black hole (Sahu et al., 2022) is microlensing. As the massive object passes in front of a star it creates magnified images of the object, total luminosity of such object will increase. Unfortunately photometric observations on their own do not allow to estimate mass of the lens. In order to infer parameters of objects taking part in the event one need to resolve images of source and trace it during the event. There is also possibility that some of the microlensing events observed by Gaia will leave visible signal in astrometric observations as for example in the case of Kruszyńska et al. (2022). Microlensing is only viable method that can be used to detect isolated black holes as such objects aren't expected to emit X-ray from interstellar medium accretion.

Recent advances in the technology allowed to open new observational window as in 2016 LIGO/VIRGO gravitational wave observatories announced discovery of first black hole - black hole merger. This was soon followed by more discoveries including black hole mergers as well as neutron star mergers. Since the beginning of the program many interesting objects have been observed contesting current knowledge about black hole formation. Up to date it was believed, that there are two forbidden regions in the black hole mass distribution: low mass gap and high mass gap. While high mass gap is the result of so called pair instability there is no consensus about the low mass gap. In the core of most massive stars temperature can reach critical value above which radiated photons can be easily converted into electron/positron pair. Such reaction can lead to decrease in the pressure resulting in implosion of stellar core. Detailed analysis (ref) suggest that due to pair instability no black holes with masses in the range ($50M_{\odot}$, $130M_{\odot}$) should exist. Lower mass gap was proposed as there are no X-ray binaries with masses of compact object in the range ($3M_{\odot}$, $5M_{\odot}$). It was contested whether it's only selection effect or there are really no black holes in this range. While there were some theoretical arguments for low mass gap (Belczynski et al., 2012) gravitational wave astronomy challenged those claims. During last years LIGO/VIRGO observed merging objects from low mass gap and high mass gap. Although it's possible that those black holes formed via merging of smaller objects origin of those objects is puzzling. Due to aforementioned discrepancies detection of black hole binaries would allow to get better insight into evolutionary channels of gravitational wave progenitors.

In recent years new approach was proposed aiming to find objects nearly filling its Roche lobe. One can expect that light curve of such object will be dominated by ellipsoidal modulation caused by tidal distortion of primary star. This approach

have great advantage due to the fact that photometric data is very vast in contrast to spectroscopic one. Relative potential of this approach was shown by (Masuda & Hotokezaka, 2019), it's estimated that light curve modulation due to ellipsoidal effect can be enough to track down at least few of them in TESS data. Other noticeable case include series of publications (Gomel et al., 2021b,a,c) on which this works is based. Publications presented new way to search for this type of objects using publicly available list of ellipsoidal variables in the direction of galactic bulge from OGLE database (Soszyński et al., 2016). This approach itself provides a rather good and robust way to look for the systems with high mass ratios. In the chapter 2 theoretical introduction to ellipsoidal modulation will be given and in the chapters it following method is employed to search for BH candidates in OGLE database.

Chapter 2

Theoretical considerations

2.1. Morris & Naftilan expression

Let's consider binary system with semi-major axis of orbit a , primary star mass M_1 and radius R_1 which is tidally disrupted by second object with mass M_2 . Traditionally one can define mass ratio $q = \frac{M_2}{M_1}$, one would like this value to be as high as possible which indicate that primary star is less massive then (hopefully unseen) companion contrary to normal convention where q is defined to be strictly smaller then 1 (assuming primary star is more massive). Up to day many publications tackled problem of ellipsoidal modulation including Kopal (1959) leading to formula proposed by Morris & Naftilan (1993)

$$\begin{aligned} \frac{\Delta L}{\bar{L}} &= \frac{\alpha_1}{\bar{L}/L_0} \left(\frac{R_1}{a} \right)^4 q (4 \sin i - 5 \sin^3 i) \cos \phi - \\ &\quad \frac{1}{\bar{L}/L_0} \left(\alpha_2 \left(\frac{R_1}{a} \right)^3 q \sin^2 i + \beta_2 \left(\frac{R_1}{a} \right)^5 q (6 \sin^2 i - 7 \sin^4 i) \right) \cos 2\varphi \\ &\quad - \frac{5}{3} \frac{\alpha_1}{\bar{L}/L_0} \left(\frac{R_1}{a} \right)^4 q \cos 3\varphi = \\ &= A_1 \cos \varphi + A_2 \cos 2\varphi + A_3 \cos 3\varphi \end{aligned} \quad (2.1)$$

where φ denotes relative phase, i inclination of orbit, L_0 is luminosity of star *without tidal disruption* while \bar{L} stands for mean luminosity of primary star. From this point onward equation 2.1 will be referred to as MN93. Coefficients α_1 , α_2 and β_2 are connected to limb darkening coefficient u and gravity darkening coefficient τ via equations

$$\alpha_1 = \frac{15u(2+\tau)}{32(3-u)}, \quad (2.2)$$

$$\alpha_2 = \frac{3(15+u)(1+\tau)}{20(3-u)}, \quad (2.3)$$

$$\beta_2 = \frac{15(1-u)(3+\tau)}{64(3-u)}. \quad (2.4)$$

Both values \bar{L} and L_0 are also related and can be found via following equation

$$\bar{L} = L_0 \left(1 + \frac{1}{9} \left(\frac{R_1}{a} \right)^3 (2 + 5q)(2 - 3 \sin^2 i) \right) \quad (2.5)$$

Equations can be rewritten in more suitable form after substitution

$$\frac{R_1}{a} = \frac{R_1}{R_{\text{Roche}}} \frac{R_{\text{Roche}}}{a} = E(q)f$$

where R_{Roche} is radius of Roche lobe, f stands for Roche lobe fillout and $E(q)$ is ratio of Roche lobe radius to semi major axis which can be described by classic Eggleton formula (Eggleton, 1983)

$$E(q) = \frac{0.49q^{-\frac{2}{3}}}{0.6q^{-\frac{2}{3}} + \log(1 + q^{-\frac{1}{3}})}. \quad (2.6)$$

MN93 equation in original form is valid only for small values of f, q making it unsuitable for any kind of search as one would like to find objects with high values of q . Following Gomel et al. (2021a) expression for second harmonic coefficient is assumed to be dominated by first term resulting in final formula

$$A_2 \approx \frac{1}{\bar{L}/L_0} \alpha_2 E(q)^3 f^3 q \sin^2 i. \quad (2.7)$$

2.2. Amplitude correction

There are few approaches one can take to extend MN93 formula, in this work original formulation from (Gomel et al., 2021b) was adopted. In original work each coefficient was multiplied by correction $C_i(q, f, i)$ computed using PHOEBE simulation software. For each fourier coefficient relevant model was fitted to PHOEBE data and then compared allowing to find such function $C(q, f, i)$ that

$$\left(C(q, f, i) - \frac{A_{\text{Phoebe}}}{A_{\text{MN93}}} \right)^2 \quad (2.8)$$

will be minimized. In Gomel et al. (2021b) following functions were chosen for second and third correction coefficients

$$C_2(q, f) = 1 + \left(0.0379 + \frac{0.005}{0.0446 + q} \right) \left(\frac{f}{1.0909 - f} \right) \quad (2.9)$$

$$C_3(q, f) = 1 + \frac{(1 + 0.0698q \sin^2 i)f^6 + 0.2075 \cdot f^2}{(2.0223 + 0.3880 \ln q)f + \sin^4 i} \quad (2.10)$$

as they have closed analytical form and small relative error.

2.3. Limitations

In previous section new corrected formula was introduced allowing to predict fourier coefficients based on physical parameters q, f, i . After correction Real light curve can be influenced by more then one modulation limiting usability of presented formula. To begin with MN93 formula is valid only for circular orbits. In order to lift that limitation one can reproduce results using other type of expansion such as Engel et al. (2020). Moreover in the case of compact binary there may be need to take into account relativistic beaming effect. Following Loeb & Gaudi (2003)

$$F_\lambda = F_{\lambda,0} \left(1 - B \frac{v_r}{c} \right) \quad (2.11)$$

where F_λ is spectral energy density, v_r radial velocity and B is coefficient defined as $B = 5 + \frac{\partial \ln F_\lambda}{\partial \ln \lambda}$. One need to emphasize that relativistic beaming effect does not affect second or third harmonic coefficient. This is purely due to the fact that beaming is caused by motion while main tidal effect is in second harmonic and can be interpreted as effect connected purely to position. This important fact makes second harmonic best for any search when the goal is to predict physical parameters based on amplitude of harmonics. There are also few other effects one can consider such as reflection effect, one can find detail analysis in Gomel et al. (2021b).

2.4. Modified mass ratio

After derivation of expression for second harmonic coefficient one can introduce *modified mass ratio* following Gomel et al. (2021a). As one can verify $A_2(q, f, i, \alpha)$ is increasing function of both $\sin i$ and f . This allows us to introduce q_{mmr} such that

$$A_2(q_{mmr}, 0.98, \pi/2, 1.2) = \tilde{A}_2 \quad (2.12)$$

where \tilde{A}_2 is measured value of second harmonic amplitude. Here $f = 0.98$ is assumed like in original approach as one aims to detect barley overflowing primary components. This definitions assures that $q \leq q_{mmr}$ is lower bound for true mass ratio for any values of i and f . This property is crucial and provide a simple way to search for objects with potentially compact companions. Second thing one need to emphasize is value of α_2 . Following original work $\alpha_2 = 1.2$ was set for observation in I band and also standard deviation $\Delta\alpha_2 = 0.1$ was assumed. This value solely represents effects of temperature, gravity and chemical composition making it very important as it's encapsulating all unknown parameters. Exact value of parameter greatly influence modified mass ratio due to which inference of mass without exact knowledge of α_2 is impossible. Detailed dependence of α_2 on the effective temperature for $\log g = 4$ based on limb and gravity darkening coefficients produced by Claret (2000) is presented on figure 2.1. This fact lead authors of method to introduce second parameter which was originally defined as 16th percentile of estimator q_{mmr} . Solely role of this parameter is to take into account

uncertainty of α acting as lower bound of q_{mmr} . In this work other parameter was introduced denoted as \tilde{q}_{mmr} and defined using equation

$$A_2(\tilde{q}_{mmr}, 0.98, \pi/2, 1.1) = \tilde{A}_2 - \Delta A_2$$

where ΔA_2 is uncertainty of estimate of A_2 coefficient. This approach not only allow to filter out those stars which can have large amplitude due to surprisingly high value of α_2 which is taken into account by decreasing α_2 in definition 2.4 to 1.1 but also allows to filter out stars that have high amplitude but also relatively high uncertainty ΔA_2 .

2.5. Selection process

In order to provide reliable and robust way to search for compact companions following procedure using aforementioned estimators of q_{mmr} was used. For each object two coefficients q_{mmr} and \tilde{q}_{mmr} were calculated and each object for which $\tilde{q}_{mmr} > 1$ was qualified as candidate for compact companion. Secondly each object with amplitude $\tilde{A}_2 > 0.24$ was removed from the list. One can find, that using 2.12 mass ratio of order $q_{mmr} \approx 1000$ is needed to obtain configuration with such great amplitude suggesting that modulation is not due to ellipsoidal effect but rather caused by other type of star variability. Exact threshold of \tilde{A}_2 can be a matter of debate due to previously mentioned dependence on α_2 which is unknown.

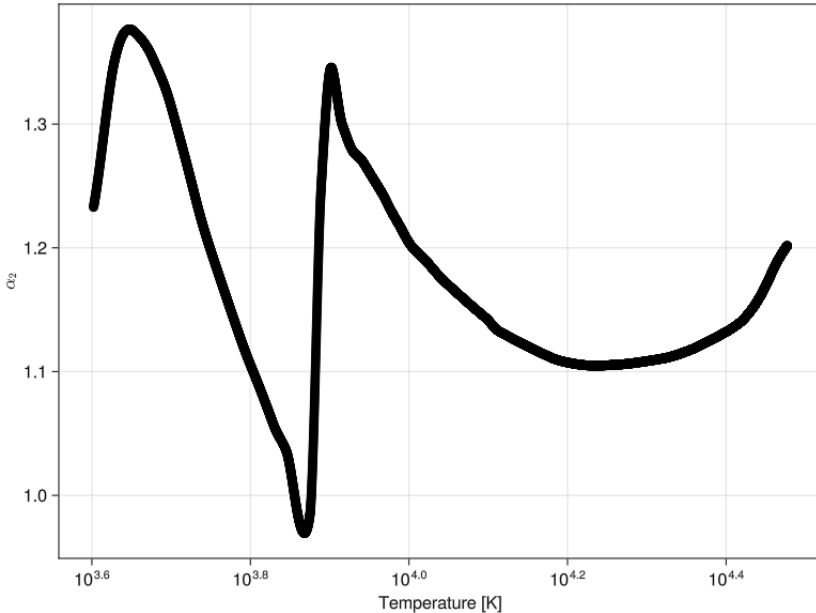


Figure 2.1: Dependence of α_2 parameter for stars with $\log g = 4$ in I band with respect to effective temperature.

Chapter 3

Observational data

3.1. Description of data and preprocessing

From OGLE database two object samples were analysed using described method. Two samples of objects were analysed in total:

- objects from the direction toward Magellanic Clouds. Sample consist of ellipsoidal stars from Pawlak et al. (2016) with objects supplemented by Przemysław Mróz,
- ellipsoidal variabales in direction toward Galactic Bulge and Galactic Disc cross-matched by Przemysław Mróz with Gaia DR3 (Collaboration et al., 2022) with $rv_amplitude_robust > 100$ km/s.

Light curves used in the analysis were collected during 4 th season of OGLE (Udalski, Szymański & Szymański (2015), Udalski, Szymanski, Kaluzny, Kubiak & Mateo (1992)) and were collected in I band. Detailed positions of objects from original samples on the sky is presented on the figure 3.1. Then for each entry nearest Gaia source was found and in case of objects with statistically significant parallax (value higher then three times it's statistical deviation) color-magnitude diagram using Gaia data was constructed and is presented on figure 3.3. Similarly color-magnitude diagram was constructed for objects without statistical significant parallax, two different plots for SMC and LMC respectively are presented on the figure 3.2. Most of the objects in the samples have relatively short period (< 3 d), detailed period distribution in is presented on the figure 3.4.

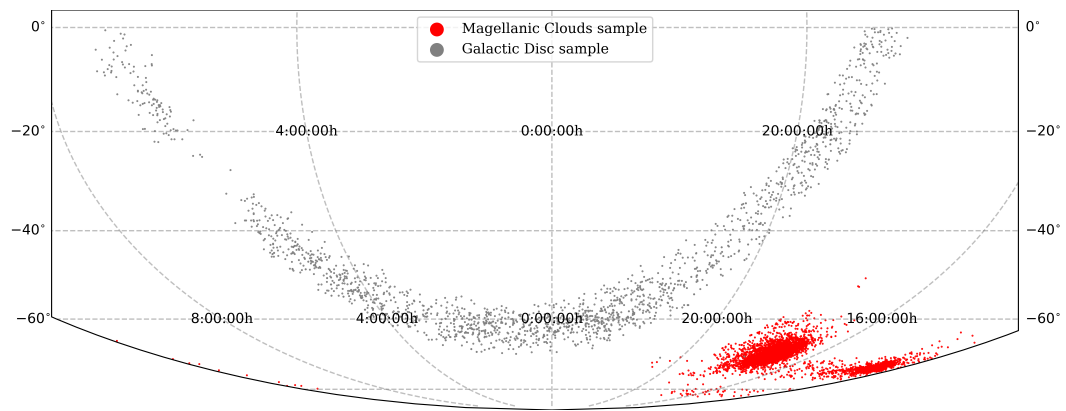


Figure 3.1: Distribution of objects in each sample.

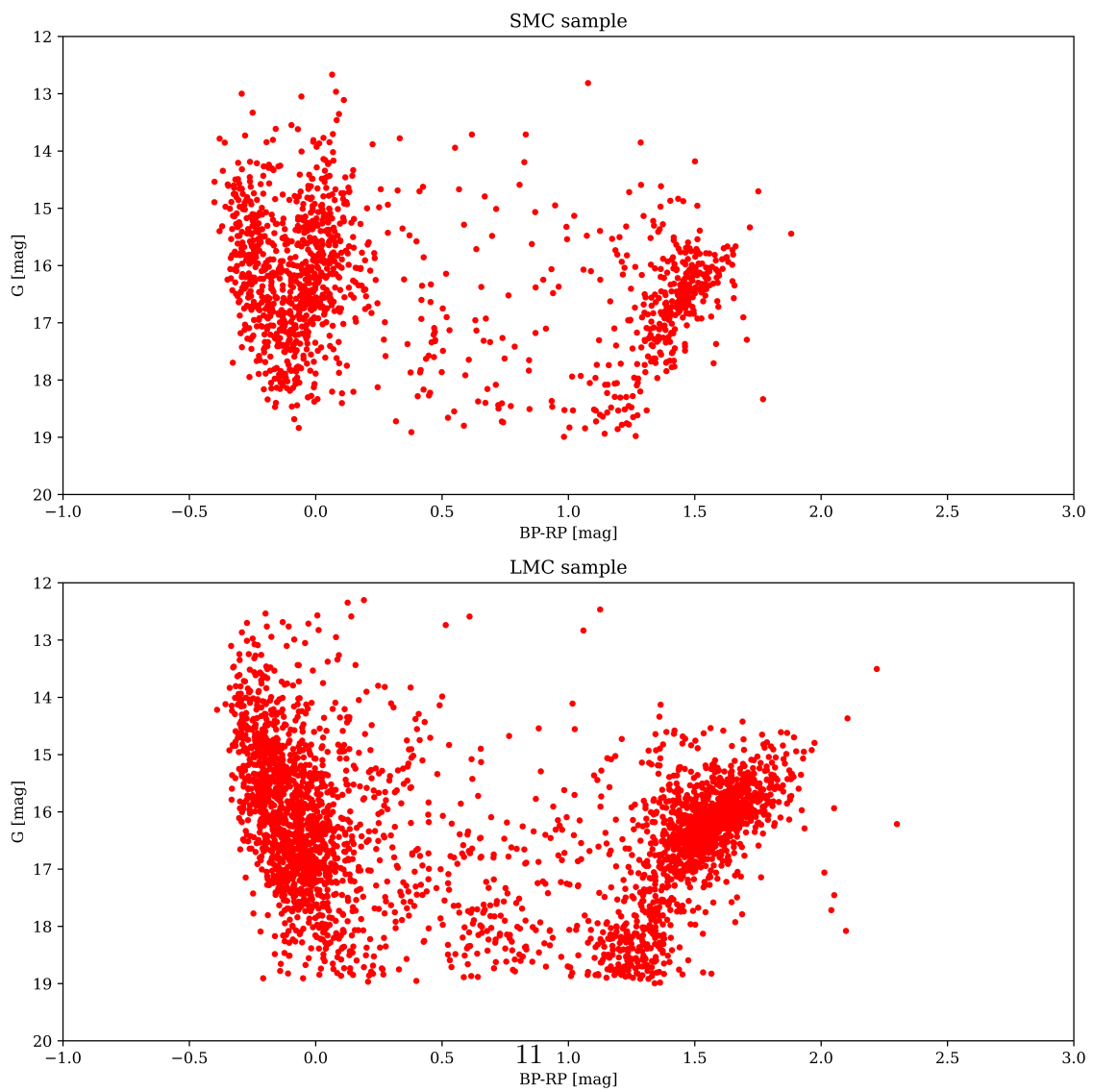


Figure 3.2: Color-magnitude diagram of Gaia counterparts potentially residing in Magellanic Clouds (without statistically significant parallax).

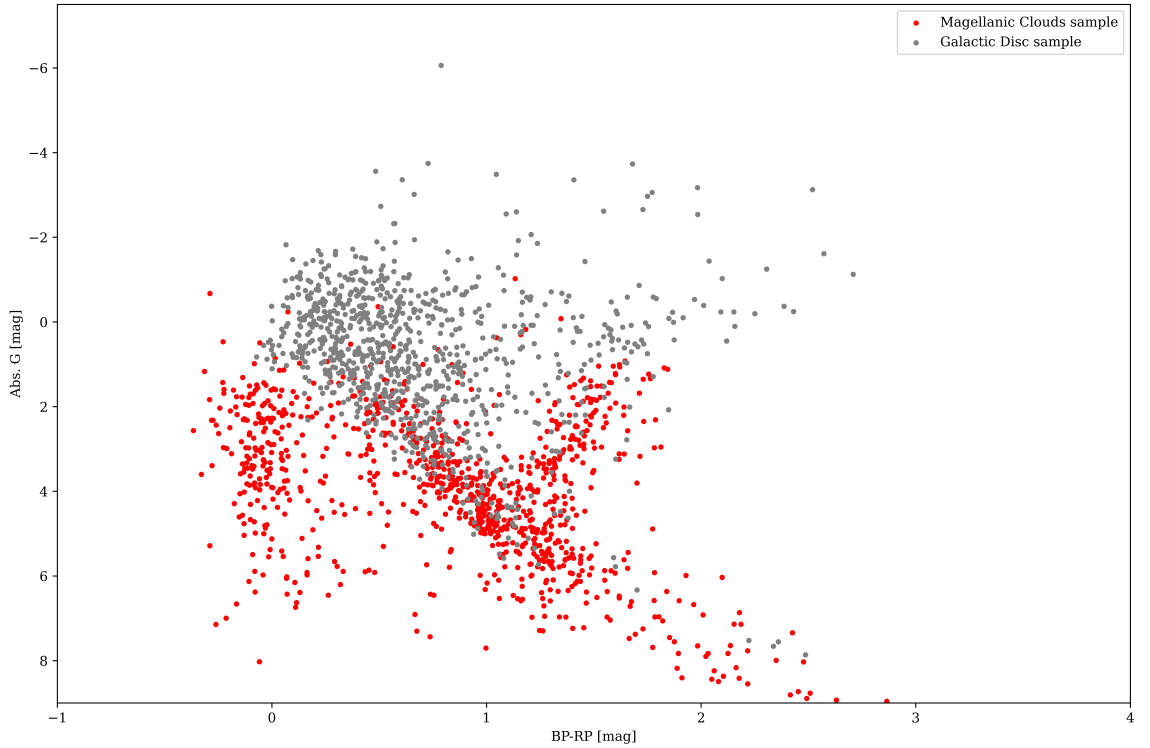


Figure 3.3: Color-magnitude diagram of Gaia counterparts with statistically significant parallax.

As first step of preprocessing objects with brightness lower than 17 mag were removed as faint stars wouldn't be suitable for radial velocity determination with usage of high resolution spectroscopy. Each object was analysed using ANOVA (analysis of variance) method (Schwarzenberg-Czerny, 1989) in order to determine period of light curve. Then each light curve was fitted with 4th degree harmonic model

$$I(t) = A_0 + \sum_{i=1}^4 \left[A_{1i} \sin \left(2\pi i \frac{t}{P} \right) + A_{2i} \cos \left(2\pi i \frac{t}{P} \right) \right] \quad (3.1)$$

with sigma clipping threshold set at 3σ allowing to determine amplitude of coefficients from the relationship $A_i = \sqrt{A_{1i}^2 + A_{2i}^2}$. Subsequently minimum mass ratio q_{mmr} together with its lower bound \tilde{q}_{mmr} were calculated and previously described procedure of selecting candidates was carried out. Objects with light curves indicating other type of variability than ellipsoidal one were removed together with those with period higher than 50 d. As according to main assumption in analysis objects should be composed of star nearly filling Roche lobe, rather short period is suggested. Exact value of threshold can be debated, here it's used as mean to remove pulsating stars that pollute sample.

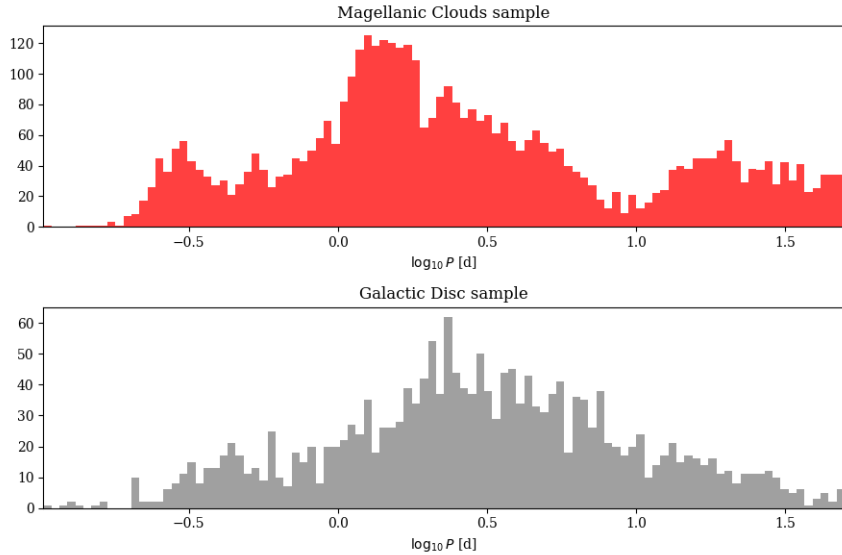


Figure 3.4: Distribution of periods from the analysed samples.

After this part of preprocessing only 41 objects from first sample left together with 22 objects from second sample.

3.2. Spectral Energy Distribution

Each object was cross matched with Gaia DR3 catalogue obtaining parallax (denoted from here as π_0 together with uncertainty denoted as σ_π) estimates of objects. If parallax was statistically significant ($\pi > 3\sigma_\pi$) it was used to derive distance to object. For objects towards Magellanic Clouds many entries lacked statistically significant parallax indicating that they really reside in Magellanic Clouds and do not line up accidentally. In this case distance estimate d_0 and distance uncertainty σ_d were based on the Jacyszyn-Dobrzeniecka et al. (2016) assuming that presented distribution of Cepheids reflects underlying distribution of stars in sample. In the case of LMC and SMC assumed distance estimates were $d_{LMC} = 49.93 \pm 1.79$ kpc and $d_{SMC} = 64.62 \pm 4.95$ kpc respectively.

To further investigate nature of objects spectral energy distribution analysis was performed with two models: single star model and double star model. Main goal of this type of analysis is to use photometry from various parts of spectra to reconstruct whole spectral characteristic and hence infer parameters (like temperature and luminosity) of object. Single star model depends on three free parameters: logarithm of temperature $\log_{10} T$ (measured in kelvins), logarithm of luminosity $\log_{10} L$ (measured in L_\odot) while third parameter was either parallax (if one was measured) or distance if it wasn't available. In the case of double star model there were two additional parameters describing second star $\log_{10} T_2$ and $\log_{10} L_2$. In the case of the first model star was assumed to be main sequence object (MS) with $\log g = 4$. In double star model primary star was

assumed to have $\log g_1 = 4$ as in the first case while second object was assumed to be a giant with $\log g_2 = 2$. Objects with statistically significant parallax were assumed to have solar like metallicity ($Z = 0.013$) as they reside inside Galactic Disc while objects in Magellanic Clouds were assumed to have metallicity equal to $Z = 0.010$ in the case of LMC/MBR and $Z = 0.005$ in the case of SMC. BaSeL library of stellar spectra (Lejeune et al., 1998) was used to find spectrum for any given $\log_{10} T$, $\log_{10} L$, d by means of interpolation as implemented in python library `pystellib`¹. Theoretically calculated stellar spectrum is then processed using `pyphot`² Python library yielding observed magnitude in required filter.

In order to find set of best fitting parameters Bayesian approach was adopted. Let's denote set of observed magnitudes as \tilde{m}_i , theoretically predicted magnitudes as m_i while errors of magnitudes as σ_i . Let's denote $\mathcal{U}(a, b)$ to be uniform distribution with support in form of interval $[a, b]$ and $\mathcal{N}(\mu, \sigma^2)$ as normal distribution with mean μ and variance σ^2 . In order to prepare Bayesian model one need to specify probability distributions that will allow to evaluate likelihood of data. Each of the observed magnitudes \tilde{m}_i is expected to be normally distributed with mean m_i and variance σ_i^2 while prior distributions on each of the three parameters is either uniform in case of $\log_{10} T$ and $\log_{10} L$ or normal in case of distance or parallax. Detailed model can be written as:

$$\begin{aligned} \log_{10} T &\sim \mathcal{U}(3.31, 4.6) \\ \log_{10} L &\sim \mathcal{U}(-3, 5) \\ d &\sim \mathcal{N}(d_0, \sigma_d^2) \text{ or} \\ \pi &\sim \mathcal{N}(\pi, \sigma_\pi^2) \\ \tilde{m}_i &\sim \mathcal{N}(m_i(\log_{10} T, \log_{10} L, d), \sigma_i^2) \text{ or} \\ \tilde{m}_i &\sim \mathcal{N}(m_i(\log_{10} T, \log_{10} L, \pi), \sigma_i^2) \end{aligned} \tag{3.2}$$

where $m_i(\log_{10} T, \log_{10} L, d)$ is written to indicate that predicted magnitude is function of parameters. Similarly one can write down second model together with priors for parameters

$$\begin{aligned} \log_{10} T_1 &\sim \mathcal{U}(3.31, 4.6) \\ \log_{10} L_1 &\sim \mathcal{U}(-3, 5) \\ \log_{10} T_2 &\sim \mathcal{U}(3.444, 4.21) \\ \log_{10} L_2 &\sim \mathcal{U}(-3, 5) \\ d &\sim \mathcal{N}(d_0, \sigma_d^2) \text{ or} \\ \pi &\sim \mathcal{N}(\pi, \sigma_\pi^2) \\ \tilde{m}_i &\sim \mathcal{N}(m_i, \sigma_i^2) \end{aligned} \tag{3.3}$$

where explicit dependence of m_i on parameters was hidden for clarity. In both cases normal distribution is truncated to positive numbers as negative parallax/distance solutions

¹<https://github.com/mfouesneau/pystellib>

²<https://github.com/mfouesneau/pyphot>

are not permitted. Range on the logarithm of temperature is limited due to boundaries of library while limit of the logarithm of luminosity is set in the boundaries in order to eliminate possible unphysical solutions. Under those assumptions log-likelihood function can be written as

$$\begin{aligned}\mathcal{L} &= - \sum_i \frac{(\tilde{m}_i - m_i)^2}{2\sigma_i^2} - \frac{(d - d_0)^2}{2\sigma_d^2} \text{ or} \\ \mathcal{L} &= - \sum_i \frac{(\tilde{m}_i - m_i)^2}{2\sigma_i^2} - \frac{(\pi - \pi_0)^2}{2\sigma_\pi^2}\end{aligned}\quad (3.4)$$

depending whether distance or parallax was used.

Following catalogues were used to assemble SEDs:

1. Catalogues shared by both samples of objects:

- 2MASS survey (Skrutskie et al., 2006),
- Gaia DR2 (Gaia Collaboration et al., 2018),
- VISTA Hemisphere Survey DR5 (McMahon et al., 2021),
- ALLWISE/WISE survey (Wright et al., (2010), Cutri et al., (2021)),
- GALEX Survey (Bianchi et al., 2011),
- Denis survey (Denis, 2005),
- SkyMapper DR1/DR2 (Wolf et al., (2018), Onken et al., (2019)),
- XMM Optical Monitor serendipitous sources catalog (Page et al., 2012).

2. Catalogues exclusive to the Magellanic Clouds sample:

- VISTA Magellanic Cloud survey DR4 (Cioni et al., 2017),
- Spitzer SAGE survey: SMC and LMC (Meixner et al., (2006), Gordon et al., (2011)),
- Denis catalogue of objects in Magellanic Clouds (Cioni et al., 2000),
- Magellanic Clouds Photometric Survey: SMC and LMC (Zaritsky et al. (2002), Zaritsky et al. (2004)).

3. Catalogues exclusive to the Galactic Disc sample:

- Bochum Galactic Disc survey (Hackstein et al., 2015),
- AAVSO Photometric All Sky Survey DR9 (Henden et al., 2015),
- VISTA Variables in Via Lactea Survey DR2 (Minniti et al., 2017),
- GLIMPSE source catalog (Spitzer Science, 2009).

In the case of magellanic clouds extinction estimates were based on the map (Skowron et al., 2021) while in the case of Galactic disc extinction was obtained using `mwdust` (Bovy et al., 2016) Python library with 3D dust map being combination of (Green et al., 2019), (Greiner et al., 2001), (Drimmel et al., 2003). In the calculations Cardelli extinction law was assumed (Cardelli et al., 1989) with $R_V = 3.1$ and python implementation from `extinction`³ was used. Using described setup MCMC python based library `emcee`⁴ (Foreman-Mackey et al., 2013) was used to construct set⁵ of routines used to sample from the posterior of models allowing to estimates parameters together with associated uncertainties. Each sampling was performed with 32 walkers for 2000 steps, in case of double model each such sampling was followed by second sampling with same parameters with starting conditions sampled from the first chain. Other packages used in the study are `astroquery` (Ginsburg et al., 2019), `corner` (Foreman-Mackey, 2016) and `astropy` (Astropy Collaboration et al., 2022). In order to help to decide between models BIC score was used

$$BIC = k \log n - 2\mathcal{L} \quad (3.5)$$

where k is number of estimated parameters and n is number of data points. From all objects 13 were selected based on high quality fit with single star model while one of the objects was selected due to observed X-ray emission that can indicate existence of accretion disc. Objects together with key parameters are listed in table 3.1.

Name	Period [d]	q_{mmr}	\tilde{q}_{mmr}	RA [deg]	DEC [deg]	A_0	A_1	A_2	A_3	A_4	π_0 [mas]
BLG986.08.7	0.5132	1.46	1.03	260.451241	-43.019464	12.192	0.0028	0.0985	0.0039	0.0093	1.20
GD2246.03.18414	0.4270	2.29	1.55	179.327372	-57.091968	12.0764	0.0045	0.1090	0.0030	0.0106	1.41
GD1097.20.23000	0.4570	9.73	5.18	252.108419	-44.137004	11.782	0.0008	0.1414	0.0029	0.0200	1.78
GD1448.27.17	1.2410	1.77	1.23	139.969949	-45.759178	11.875	0.0115	0.1035	0.0030	0.0056	0.77
BLG931.27.36745	0.7050	2.44	1.63	261.74489	-40.31792	11.633	0.0033	0.1113	0.0026	0.0105	1.46
GD1070.18.22288	45.1467	7.41	3.73	257.007546	-41.048747	11.369	0.0091	0.1362	0.0043	0.0049	1.03
LMC574.11.3407	0.2551	1.48	1.03	80.1415	-63.185667	16.919	0.0064	0.0989	0.0013	0.0092	0.45
LMC606.30.48	0.2698	1.67	1.11	92.27575	-63.376167	15.906	0.0141	0.1019	0.0038	0.0122	0.52
LMC751.15.2886	0.3753	1.70	1.16	98.082958	-66.307861	16.958	0.0090	0.1024	0.0012	0.0121	0.18
MBR108.18.3	0.2947	1.49	1.02	33.257292	-72.993167	13.376	0.0063	0.0989	0.0033	0.0128	1.10
MBR236.09.433	0.4398	1.51	1.07	50.642958	-80.540667	14.585	0.0024	0.0994	0.0028	0.0089	0.47
SMC711.22.1068	0.4466	2.35	1.56	9.833875	-70.378028	13.226	0.0029	0.1104	0.0053	0.0154	0.66
SMC720.28.40576	0.5674	4.29	2.56	11.938042	-73.13625	16.367	0.0017	0.1246	0.0037	0.0035	—
SMC742.26.330	0.3453	1.68	1.12	350.85925	-77.530417	13.864	0.0042	0.1020	0.0049	0.0074	1.07

Table 3.1: Selected objects together with period, estimated mass ratios, coordinates, fourier coefficients (A_i) and parallax from Gaia DR3

What should be emphasised here is meaning of BIC score. As little is assumed about objects especially best fitting $\log g/Z$ is not investigated which can be crucial to obtain high quality spectral fit. Due to this effect it's unreasonable to calculate values

³<https://extinction.readthedocs.io/en/latest/index.html>

⁴<https://emcee.readthedocs.io/en/stable/>

⁵<https://github.com/Wesenheit/Iris>

of χ^2 and compare them across objects as few of them can be better fitted with given metallicity/ $\log g$. Single model SED fits together with light curves are presented in appendix A. Each subsection consists of phased light curve, SED fit plot, corner plot for posterior distribution and other relevant data.

Chapter 4

Results

4.1. Physical parameters of objects

Each of 14 final object was further investigated using available data in order to determine physical properties of objects. Out of all 14 objects 12 of are of spectral types G or F, one object is of spectral type O while last one is composed of two objects. 13 stars from the list have measured parallax from Gaia DR3 while one of the objects is located in SMC. 11 objects were selected based on good fit with single star model while one was selected due to counterpart emission in X-ray.

For each entry mass of object was estimated using PARSEC (Bressan et al., 2012) evolutionary tracks. Assuming solar like metallicity simple approximate fits were obtained by choosing best fitting entry from PARSEC track using temperature and luminosity estimates from SED fits.

Name	T [K]	$\log_{10} L/L_\odot$	$E(B - V)$	d [kpc]	BIC	M_{PARSEC} [M_\odot]
BLG986.08.7	6190^{+26}_{-25}	$0.825^{+0.011}_{-0.012}$	0.226	0.83 ± 0.01	729.8	1.4
GD2246.03.18414	6974^{+21}_{-28}	0.806 ± 0.008	0.273	0.71 ± 0.01	586.3	1.4
GD1097.20.23000	6126 ± 13	$0.626^{+0.007}_{-0.006}$	0.221	0.56 ± 0.008	197.8	1.2
GD1448.27.17	8516^{+59}_{-64}	1.863 ± 0.013	0.611	1.30 ± 0.02	215.8	2.3
BLG931.27.36745	6416 ± 10	$0.901^{+0.044}_{-0.041}$	0.199	$0.69^{+0.04}_{-0.03}$	206.1	1.4
LMC574.11.3407	4740 ± 24	$-0.349^{+0.153}_{-0.124}$	0.034	$2.21^{+0.42}_{-0.29}$	849.3	—
LMC606.30.48	5516 ± 25	-0.053 ± 0.066	0.047	$1.93^{+0.15}_{-0.13}$	184	0.8
LMC751.15.2886	6068 ± 23	$0.392^{+0.342}_{-0.241}$	—	$5.39^{+2.60}_{-1.31}$	470.3	1.1
MBR108.18.3	5884 ± 6	0.228 ± 0.011	—	0.91 ± 0.01	3333.3	1.0
MBR236.09.433	6471 ± 10	0.717 ± 0.027	—	2.12 ± 0.07	592.1	1.4
SMC711.22.1068	6771 ± 5	$0.852^{+0.017}_{-0.015}$	0.021	1.52 ± 0.03	707.4	1.4
SMC720.28.40576	34079^{+536}_{-496}	$4.366^{+0.069}_{-0.071}$	0.095	—	168.8	16
SMC742.26.330	5808 ± 6	0.356 ± 0.010	—	0.93 ± 0.01	2539.4	1

Table 4.1: Estimated physical parameters of objects using single star model together with PARSEC mass estimates and extinction estimates.

4.2. Radial velocity semi-amplitude estimation from Gaia DR3 data

Half of the objects from final list have available high-quality radial velocity information that is normally computed for bright stars from Gaia DR3 catalogue. While estimate of radial velocity is based on median of observed radial velocity, error of this estimate is based on the epoch standard deviation of observed values. According to (Katz et al., 2022) radial velocity error δv is calculated via equation

$$\delta v = \sqrt{\sigma_{med}^2 + 0.11^2} \quad (4.1)$$

$$\sigma_{med} = \sqrt{\frac{\pi}{2} \frac{\sigma(V_j)}{\sqrt{N}}} \quad (4.2)$$

where $\sigma(V_j)$ is standard deviation of radial velocity while N stands for number of transits used to compute radial velocity. This simple formula allows to obtain variance of radial velocity measurements as

$$\sigma^2 = \frac{2N}{\pi} ((\delta v)^2 - 0.11^2). \quad (4.3)$$

It can be proven (for details see appendix B) that if one assume error is dominated by sinusoidal radial movement with amplitude K variance of velocity will be equal to

$$\sigma^2 = \frac{K^2}{2}. \quad (4.4)$$

This observation can be used to estimate semi-amplitude of velocity using Gaia measurements (that will be denoted from here as K_{Gaia}) as

$$K_{Gaia} = \sqrt{\sigma^2} \sqrt{2} = 2 \sqrt{\frac{N}{\pi} ((\delta v)^2 - 0.11^2)} \quad (4.5)$$

This radial velocity amplitude then is used to calculate binary mass function for each of objects using definition

$$f(M_1, M_2, i) = \frac{M_2^3 \sin i^3}{(M_1 + M_2)^2} = \frac{K^3 P}{2\pi G} \quad (4.6)$$

where P stands for period while G is gravitational constant. For each object with RV estimates based on aforementioned method mass functions were obtained and together with information about radial velocity estimates are presented in table 4.2. For each object with PARSEC mass estimate lower boundary of companions mass was calculated by solving equation 4.6 with $\sin(i) = 1$. Each of minimum masses were then plotted versus period of binary and are presented on ?? and placed into table as M_{min} .

In (Katz et al., 2022) criterion was presented allowing to test whether radial velocity indicates variability based on values of rv_chisq_pvalue and $rv_renormalised_gof$. Criterion states that objects with $N > 10$, $T_{eff} \in [3900, 8000]$ K, $rv_chisq_pvalue < 0.01$

and $rv_renormalised_gof > 4$ can be safely considered to be variable in radial velocity. Each object was tested using described method and only two entries (BLG931.27.36745 and GD1097.20.23000) cannot be safely assumed to be variable in radial velocity as they weren't observed enough times.

Name	Period [d]	RV [km/s]	N	δv [km/s]	K_{Gaia} [km/s]	$f(M_1, M_2, i)$ [M_\odot]	M_{min} [M_\odot]
GD2246.03.18414	0.4270	27.68	25	23.03	129.93	0.097	0.77
GD1097.20.23000	0.4570	36.5	10	21.03	75.03	0.020	0.37
BLG986.08.7	0.5132	-1.69	15	18.11	79.14	0.026	0.43
BLG931.27.36745	0.7050	-4.35	8	14.81	47.26	0.0077	0.28
GD1448.27.17	1.2410	33.08	22	7.69	40.69	0.0086	0.40
GD1070.18.22288	45.1467	38.71	20	7.66	38.65	0.27	-

Table 4.2: Estimated mass function using Gaia radial velocity error.

4.3. Detailed analysis of objects

In this section detailed characteristic of individual objects will be provided. It will be divided into 3 subsections where first two will quickly cover information available for objects GD1070.18.22288 and SMC720.28.40576 while third one will be dedicated to rest.

4.3.1. GD1070.18.22288

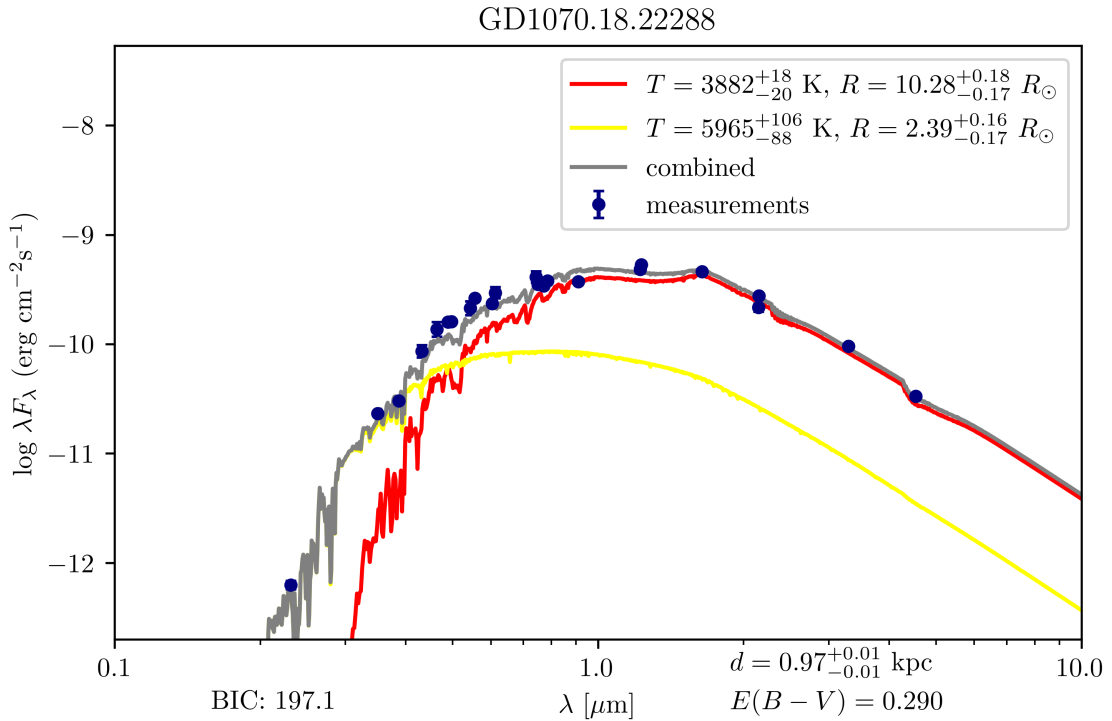
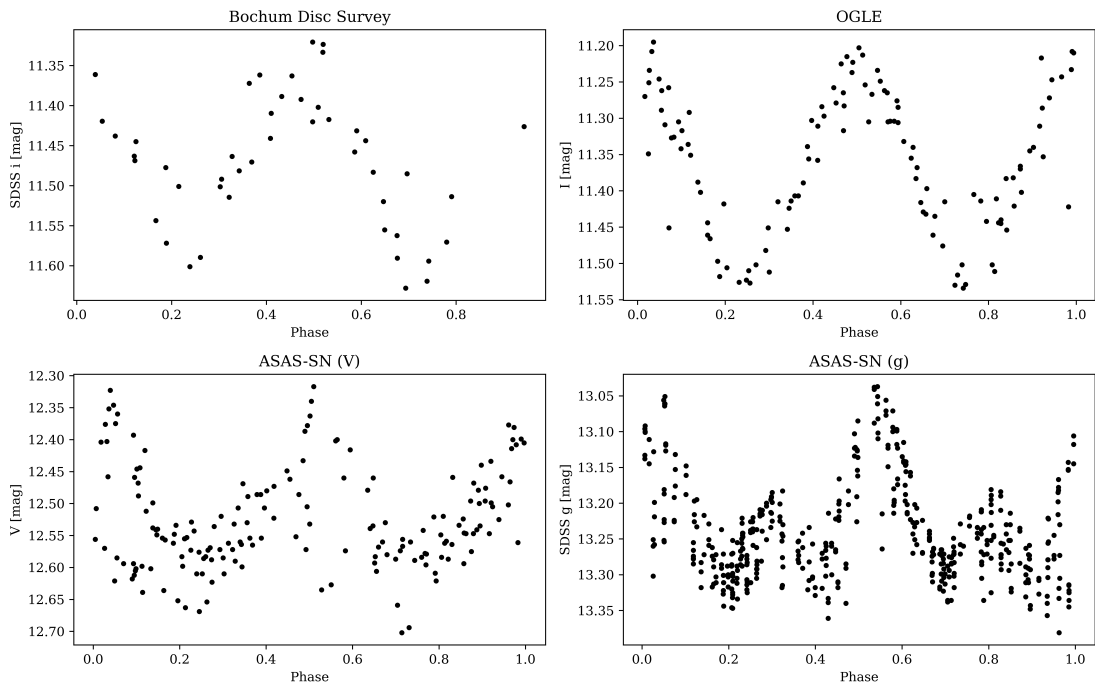


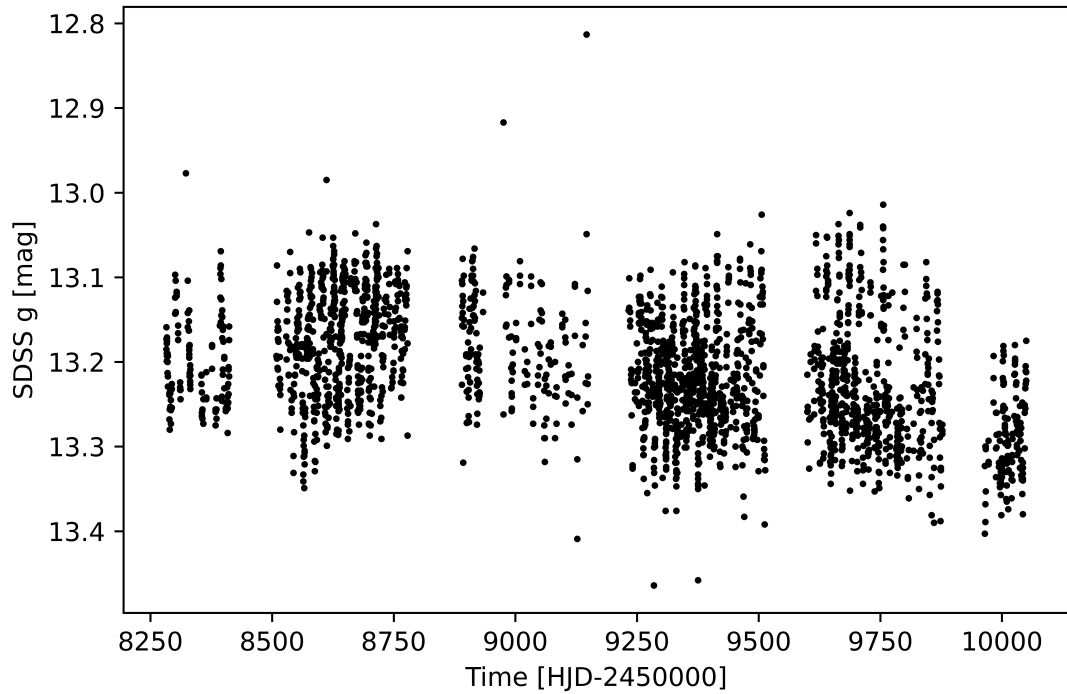
Figure 4.1: Spectral Energy Distribution fit for GD1070.18.22280 using model with two components.

GD1070.18.22280 has longest period from selected objects with $P \approx 45$ d and was listed as plausible candidate only due to the reported X-ray emission. Due to excess amount of observations in many parts of spectra it was possible to obtain high quality spectral energy distribution fit that revealed two sources with different temperatures, presented distribution can be seen on plot 4.1. One of the objects with rather low temperature of $T \approx 3800$ K has radius $R \approx 10 R_\odot$ and was quite distant from any evolutionary track in PARSEC database as it's probably giant stripped by it's companion. Object can be also found in ASAS-SN database (Jayasinghe et al., 2019) under id J170801.81-410255.6 where it's classified as rotational variable star with half of the period found in this work. It was observed by ASAS-SN in V and SDSS g band allowing to compare light curves with OGLE. Moreover it was observed in SDSS i band by Bochum Disc Survey (Hackstein et al., 2015). Comparison between all light curves can be found on the plot 4.2a ASAS-SN observation in g band can be traced back to 2016 and allow to get better insight into evolution of light curve over time, change of observed brightness is presented on the plot 4.2b. Object have also greatest value of mass function from whole sample that is equal to $\sim 0.25 M_\odot$.

GD1070.18.22288



(a) Light curves of GD1070.18.22288 in 4 different bands



(b) Change of brightness in SDSS g band over time

Object was observed in X-ray by Swift and XMM missions and published in serendipitous sources catalogs (Evans et al. (2020) and Traulsen et al. (2020)) with id names J170801.8-410254 and J170801.8-410255 respectively. Angular distance between position reported by XMM DR11 catalogs (Traulsen et al., 2020) and OGLE position is 105 mas and has reported statistical/positional error of order 365 mas. This area of galactic disc also came to attention due to gamma ray source source HESS J1708-410 (Aharonian et al., 2008) located 4.212 arcminutes from estimated OGLE position. Gamma emission have extended character and position reported by OGLE falls near 1σ region of emission center. Up to date no plausible explanation was found to the origin of aforementioned source despite multiple efforts and search in various parts of optical spectra. One particular work (Van Etten et al., 2009) observed close neighbourhood of gamma ray source and found emission from point source labeled in the publication as nr 1 (hereinafter referred to as [VFH2009] 1). This particular point source although quite faint coincides with position of GD1070.18.22280 with accuracy of 382 mas. In the publication it was found that X-ray emission is best fitted with absorbed power law by hydrogen density $n_H = 2.0 \times 10^{21} \text{ cm}^{-2}$. Interestingly assumed distance of 3 kpc based on radio observations is nearly 3 times higher then one obtained using parallax from Gaia DR3. Based on the Gaia parallax measurements one can estimate X-ray luminosity of object to $L_X = 1.32 \cdot 10^{31} \text{ erg/s}$.

As one can see on figure 4.2a there is discrepancy between curves in I band and curves from ASAS-SN. This is due to the different time light curves were collected. OGLE light curve is composed from observations collected from 2456467 to 2458734 HJD but most samples were collected before 2457201 HJD. On the other hand observations from ASAS-SN in g band were collected after 2459797 HJD. Using archival data from ASAS-SN there is visible point around 2459100 when period of the variable changes from ~ 45 d to nearly half the value around ~ 22.4 d. This observation together with evolution of amplitude of the variability as presented on the plot 4.2b clearly suggest that object represents class of rotational variables. This can be also partially supported by the X ray emission from the system, it's widely known that many rotational variables like RS Canum Venaticorum can emit X rays with luminosity around $\sim 10^{31} \text{ erg/s}$ (Walter et al., 1980) so value obtained from XMM is consisted with emission from this type of system. It's hard to determine if OGLE curve exhibit similar changes in brightness as observations cover only relatively short period of time. It's highly unlikely that variability in I band is caused by ellipsoidal modulation if period would be equal to 45 d as inferred radii are to small for the system to fill their Roche Lobes (unless system would have very small total mas). After investing all of the observational data it's hard to pinpoint true nature of the system. Most plausible explanation states that the system is similar to RS Canum Venaticorum variable which underwent mass transfer in the past. Colder star is covered in spots that emerge due to high magnetic fields, such stars can develop powerful coronal heating responsible for X-ray emission. Although one could investigate spectrum of object to find whether it's consisted with emission from hot plasma, since although object isn't ellipsoidal variable this line of investigation is dropped as it's beyond scope of the work.

4.3.2. SMC720.28.40576

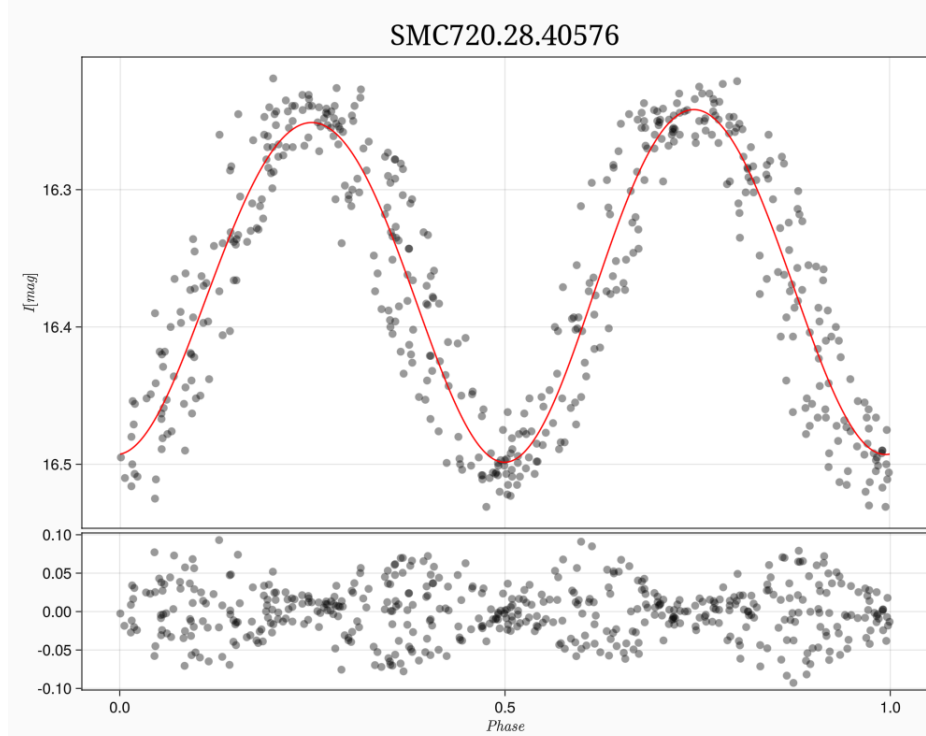


Figure 4.3: Light curve of SMC720.28.40576 collected by project OGLE.

SMC720.28.40576 is the only object in the sample that reside in Magellanic Clouds. It's very luminous and hot, estimated parameters suggest it's blue giant with spectral type O according to single model SED fit 4.4. Estimated period of the variable is nearly half of day, such short period paired together with such high mass suggest very compact setup of stars. PARSEC evolutionary tracks estimate mass of object around $16 M_{\odot}$. Star was published already by (Pawlak et al., 2016) and classified as contact binary. Although no companion is visible in SED distribution it might hide itself in the light of primary star. No WISE source could be found as nearest detection is nearly 10 arcsec away from the position, lack of any observations in W3 and W4 bands is very problematic as they allow to probe object in low temperatures. No radial velocity from Gaia is available so mass function estimate remains unknown.

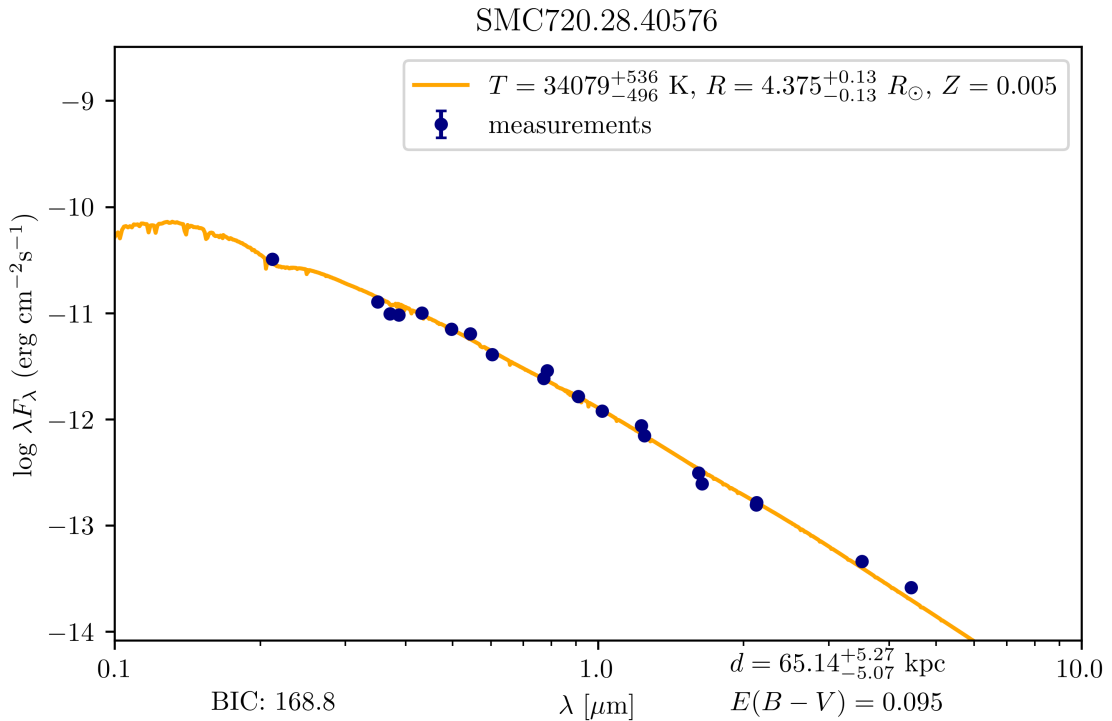


Figure 4.4: Single model SED fit for SMC720.28.40576.

Available data paired with MCMC allow to put some constrains on the parameters of objects even if chain had not converged. When MCMC chain isn't able to determine significance of some parameters it's reconstructing prior distribution which results in uniformly distributed region of samples. If for some set of parameters predicted probability is very small such region shouldn't be populated by samples resulting in the uniformly region where any possible companion star can reside. Second MCMC run was performed and 64000 samples were drawn from posterior distribution. SED fit is performed assuming $\log g_1 = 4$ and $\log g_2 = 4$ as one expect secondary component to be main sequence star. Results of MCMC sampling were plotted over samples from HYG database¹ and are presented on figure 4.5

¹<https://www.astronexus.com/hyg>

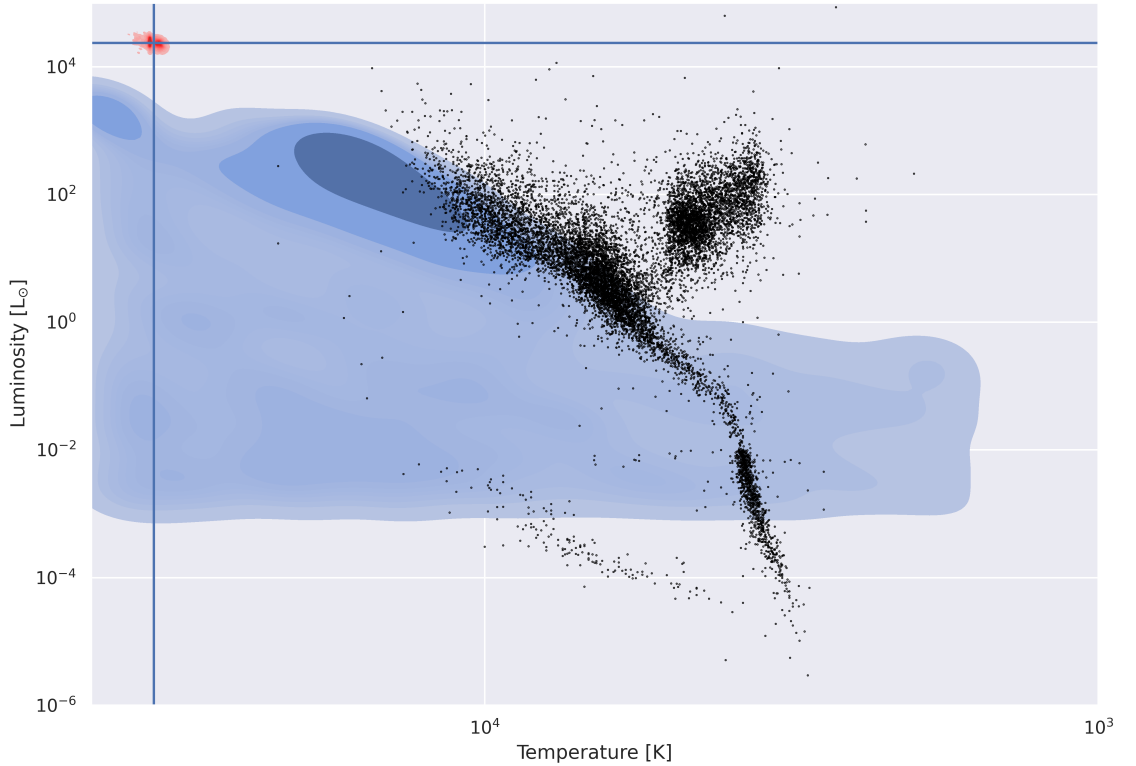


Figure 4.5: Posterior estimate for parameters of SMC720.28.40576 highlighted in red (primary component) and in blue (secondary component).

One can see, that samples fill the space almost uniformly but omit region populated with cold and luminous stars as those are to luminous in infrared to reproduce observed values. Although any objects on giant branch can be ruled out many regions on HR diagram can host potential secondary companion, most importantly few regions of main sequence stars aren't excluded giving plausible candidate for secondary companion.

4.3.3. Rest of objects

Majority of objects on the list can be characterized as objects with intermediate temperature. They typically have radius in order of few solar radii and spectral type from G to A. Although no detailed information about objects was found two of them are listed as non-single stars in Gaia DR3 Eclipsing Binaries catalog (BLG986.08.7, BLG931.27.36745). Catalog contains stars with collected light curves that matched precomputed set of eclipsing/ellipsoidal binaries. Detailed processing steps can be found in Gaia documentation¹. After matching the light curve with precomputed set best model serves as start in local optimiser trying to further refine solution. Model is solved with respect to parameters:

¹https://gea.esac.esa.int/archive/documentation/GDR3/Data_analysis/chap_cu4nss/sec_cu4nss_eclipsing_bin/

- fillout factors of stars s_1 , s_2 ,
- inclination i ,
- temperature ratio T_1/T_2 (effective values),
- argument of periastron ω ,
- time t_0 of eclipse.

Both objects reported by Gaia DR3 are fitted with contact binary model where $s_1 > 1$ and $s_2 > 1$ with almost no temperature difference (ratio close to 1). This results pointed out that it's possible to obtain similar results in the contact system with same temperature for both stars fooling SED fit.

This line was further investigated and each object was fitted using PHOEBE simulation software (Wilson & Devinney (1971), Prša & Zwitter (2005), Conroy et al., (2020)). Model was constructed in such way that both stars shared temperature T (inferred from single model SED) and were overflowing their Roche lobes. Two masses together with inclination i and radius of primary star R_1 form four parameters that are fitted to minimize χ^2 using Nelder-Mead algorithm. Second radius is no longer free parameter and it's constrained by common envelope. Fitted values together with χ^2 values are presented in the table 4.3 together with predicted semi-amplitude of velocity together with estimated one if available from Gaia DR3 data.

Name	M_1 [M_\odot]	M_2 [M_\odot]	R_1 [R_\odot]	R_2 [R_\odot]	i	K_{estimate} [km/s]	K_{Gaia} [km/s]	χ^2/dof
BLG931.27.36745	1.03	0.31	1.88	1.21	57.67°	50.71	47.26	513.67/74
GD1097.20.2300	1.14	0.37	1.56	1.02	55.74°	64.05	75.03	2929.66/118
BLG986.08.7	1.43	0.43	1.82	1.15	46.52°	55.17	79.14	827.58/72
GD2246.03.1814	1.09	0.34	1.45	0.92	50.63°	58.42	129.93	1426.90/124
GD1448.27.17	1.58	0.75	2.99	2.16	55.39°	69.52	40.69	4391.59/184

Table 4.3: Table with parameters used to fit light curves of objects together with radial velocities estimates and normalized χ^2 values.

One example light curve fit for object BLG931.27.36745 can be seen on the plot 4.6. Few of the light curves can be well fitted using contact light curve model like BLG931.27.36745 or BLG986.08.7 where light curve matches observed values very well but also velocity in such binary is close or very close to the value obtained from Gaia. In some cases like GD1097.20.2300 or GD1448.27.17 there is some room for improvement, there are some discrepancies between model and observed curves. Values obtained from the fit can be quite distant from reality there is not enough data to constrain parameters of the model. Despite this fact as demonstrated not only some of the objects can be

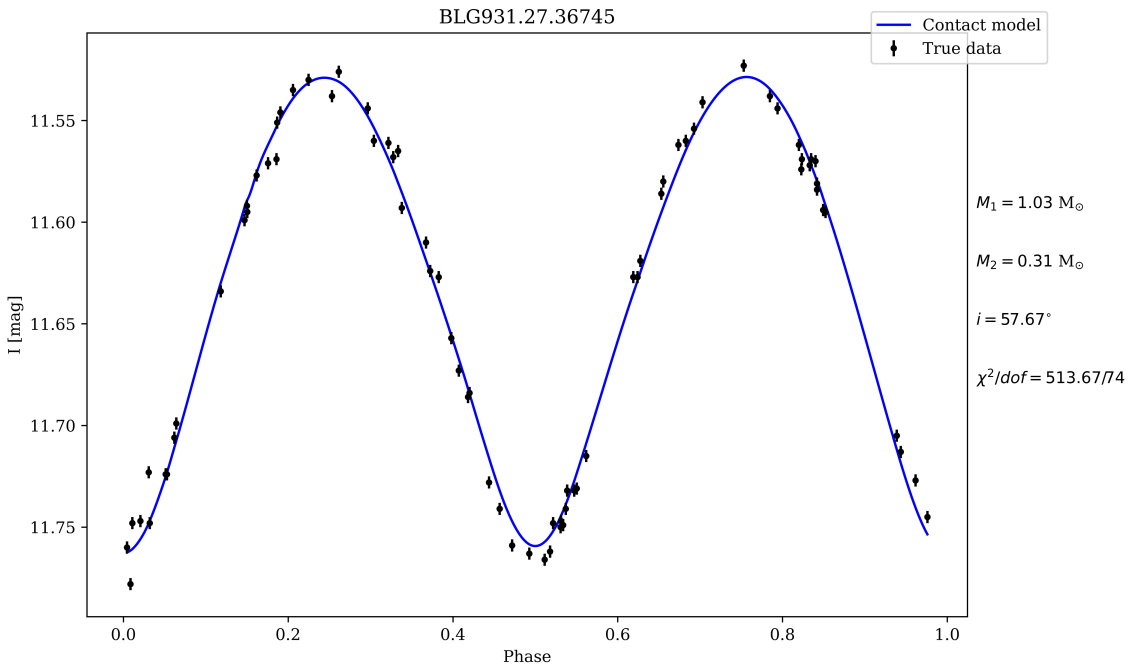


Figure 4.6: Light curve fit with contact binary for BLG931.27.36745 calculated using PHOEBE.

well described using contact model but one can see that in all cases contact model can achieve amplitude comparable to real one. This indicates great weakness of method described in Gomel et al. (2021c) as simple contact binary can easily be classified as potential candidate.

Chapter 5

Discussion

Out of total 8515 objects investigated in this study only 14 objects were classified as plausible candidates for binaries with compact companions. Further investigation into sample revealed one rotational variable and suggested alternative explanation for 12 objects in the form of contact binaries with intermediate mass ratio. For 7 objects mass function was calculated and revealed no interesting objects as for most of them $f(m_1, m_2, i) < 0.1 M_{\odot}$. Only object with higher mass function is GD1070.18.22288 which is likely rotational variable with unknown orbital period resulting in useless mass function. It's hard to determine what is accuracy of mass function estimation which can be skewed by many factors. Those doubts begin to strengthen if one assume that objects are composed of two stars with similar temperature as suggested by light curve analysis. In this case it's unknown what to expect as spectra of objects are composed of two base objects which can be hard to process by Gaia pipeline. Up to date only one work (Nagarajan et al., 2023) tries to perform any kind of follow-up observations of candidate BH binaries reported in (Gomel et al., 2022) which were identified using method presented in (Gomel et al., 2021b). This publication is one step ahead with respect to this work as spectroscopic follow-up was performed allowing to estimate amplitude of velocity with much higher precision then very crude estimation based on Gaia DR3 radial velocity measurements. Nevertheless presented results match those presented in the work as most of the objects share many physical parameters. It was pointed out that method used to identify objects is based on the assumption that objects nearly fill their Roche Lobes what occurs during relatively short period of binaries lifetime. Contact binaries although rare outcome of evolution are expected to be quite common compared to any kind of compact objects. Light curve modeling with contact binaries isn't able to explain all of variability so fit might need some refining but even if contact model fails in some cases it's still provides quite good explanation for observed variability. Most importantly estimated amplitude of such modulation can easily reach values set at threshold for which $q_{mmr} > 1$ resulting in huge number of false positives. Although no final conclusion is reached results seem to support conclusion of (Nagarajan et al., 2023). In order to further characterize objects more observations should be conducted.

Bibliography

- Aharonian F., et al., 2008, *Astronomy & Astrophysics*, 477, 353
- Astropy Collaboration et al., 2022, *The Astrophysical Journal*, 935, 167
- Belczynski K., Wiktorowicz G., Fryer C. L., Holz D. E., Kalogera V., 2012, *The Astrophysical Journal*, 757, 91
- Belloni T. M., Motta S. E., 2016, in Bambi C., ed., , Vol. 440, *Astrophysics of Black Holes*. Springer Berlin Heidelberg, Berlin, Heidelberg, pp 61–97, doi:10.1007/978-3-662-52859-4_2, http://link.springer.com/10.1007/978-3-662-52859-4_2
- Bianchi L., Herald J., Efremova B., Girardi L., Zabot A., Marigo P., Conti A., Shiao B., 2011, *Astrophysics and Space Science*, 335, 161
- Bovy J., Rix H.-W., Green G. M., Schlafly E. F., Finkbeiner D. P., 2016, *The Astrophysical Journal*, 818, 130
- Bressan A., Marigo P., Girardi L., Salasnich B., Dal Cero C., Rubele S., Nanni A., 2012, *Monthly Notices of the Royal Astronomical Society*, 427, 127
- Brown G. E., Bethe H. A., 1994, *The Astrophysical Journal*, 423, 659
- Cardelli J. A., Clayton G. C., Mathis J. S., 1989, *The Astrophysical Journal*, 345, 245
- Cioni M.-R., et al., 2000, *Astronomy and Astrophysics Supplement Series*, 144, 235
- Cioni M. R. L., et al., 2017, *VizieR Online Data Catalog*, p. II/351
- Claret A., 2000, *Astronomy and Astrophysics*, 363, 1081
- Collaboration G., et al., 2022,] 10.48550/ARXIV.2208.00211
- Conroy K. E., et al., 2020, *The Astrophysical Journal Supplement Series*, 250, 34
- Corral-Santana J. M., Casares J., Muñoz-Darias T., Bauer F. E., Martínez-Pais I. G., Russell D. M., 2016, *Astronomy & Astrophysics*, 587, A61
- Cutri R. M., et al., 2021, *VizieR Online Data Catalog*, p. II/328

- Denis C., 2005, VizieR Online Data Catalog, p. B/denis
- Drimmel R., Cabrera-Lavers A., Lopez-Corredoira M., 2003, *Astronomy & Astrophysics*, 409, 205
- Eggleton P. P., 1983, *The Astrophysical Journal*, 268, 368
- El-Badry K., et al., 2022, *Monthly Notices of the Royal Astronomical Society*, 518, 1057
- Engel M., Faigler S., Shahaf S., Mazeh T., 2020, *Monthly Notices of the Royal Astronomical Society*, 497, 4884
- Evans P. A., et al., 2020, *The Astrophysical Journal Supplement Series*, 247, 54
- Foreman-Mackey D., 2016, *The Journal of Open Source Software*, 1, 24
- Foreman-Mackey D., Hogg D. W., Lang D., Goodman J., 2013, *Publications of the Astronomical Society of the Pacific*, 125, 306
- Gaia Collaboration et al., 2018, *Astronomy & Astrophysics*, 616, A1
- Ginsburg A., et al., 2019, *The Astronomical Journal*, 157, 98
- Gomel R., Faigler S., Mazeh T., 2021a, *Monthly Notices of the Royal Astronomical Society*, 501, 2822
- Gomel R., Faigler S., Mazeh T., 2021b, *Monthly Notices of the Royal Astronomical Society*, 504, 2115
- Gomel R., Faigler S., Mazeh T., Pawlak M., 2021c, *Monthly Notices of the Royal Astronomical Society*, 504, 5907
- Gomel R., et al., 2022, *Astronomy & Astrophysics*
- Gordon K. D., et al., 2011, *The Astronomical Journal*, 142, 102
- Green G. M., Schlaflly E., Zucker C., Speagle J. S., Finkbeiner D., 2019, *The Astrophysical Journal*, 887, 93
- Greiner J., Cuby J. G., McCaughrean M. J., 2001, *Nature*, 414, 522
- Hackstein M., et al., 2015, *Astronomische Nachrichten*, 336, 590
- Henden A. A., Levine S., Terrell D., Welch D. L., 2015, 225, 336.16
- Jacyszyn-Dobrzeniecka A. M., et al., 2016, *Acta Astronomica*, 66, 149
- Jayasinghe T., et al., 2019, *Monthly Notices of the Royal Astronomical Society*
- Katz D., et al., 2022, Gaia Data Release 3 Properties and validation of the radial velocities, <http://arxiv.org/abs/2206.05902>

- Kopal Z., 1959, Close binary systems. <https://ui.adsabs.harvard.edu/abs/1959cbs..book.....K>
- Kreidberg L., Bailyn C. D., Farr W. M., Kalogera V., 2012, The Astrophysical Journal, 757, 36
- Kruszyńska K., et al., 2022, Astronomy & Astrophysics, 662, A59
- Lasota J.-P., 2001, New Astronomy Reviews, 45, 449
- Lejeune T., Cuisinier F., Buser R., 1998, Astronomy and Astrophysics Supplement Series, 130, 65
- Lennon D. J., Dufton P. L., Villaseñor J. I., Evans C. J., Langer N., Saxton R., Monageng I. M., Toonen S., 2022, Astronomy & Astrophysics, 665, A180
- Liu J., et al., 2019, Nature, 575, 618
- Loeb A., Gaudi B. S., 2003, The Astrophysical Journal, 588, L117
- Masuda K., Hotokezaka K., 2019, The Astrophysical Journal, 883, 169
- McMahon R. G., Banerji M., Gonzalez E., Koposov S. E., Bejar V. J., Lodieu N., Rebolo R., VHS Collaboration 2021, VizieR Online Data Catalog, p. II/367
- Meixner M., et al., 2006, The Astronomical Journal, 132, 2268
- Minniti D., Lucas P., VVV Team 2017, VizieR Online Data Catalog, p. II/348
- Morris S. L., Naftilan S. A., 1993, The Astrophysical Journal, 419, 344
- Nagarajan P., El-Badry K., Rodriguez A. C., van Roestel J., Roulston B., 2023, Spectroscopic follow-up of black hole and neutron star candidates in ellipsoidal variables from Gaia DR3, <http://arxiv.org/abs/2304.07324>
- Onken C. A., et al., 2019, Publications of the Astronomical Society of Australia, 36, e033
- Page M. J., et al., 2012, Monthly Notices of the Royal Astronomical Society, 426, 903
- Pawlak M., et al., 2016, Acta Astronomica, 66, 421
- Prša A., Zwitter T., 2005, The Astrophysical Journal, 628, 426
- Sahu K. C., et al., 2022, The Astrophysical Journal, 933, 83
- Schwarzenberg-Czerny A., 1989, Monthly Notices of the Royal Astronomical Society, 241, 153
- Shenar T., et al., 2022, Nature Astronomy, 6, 1085
- Skowron D. M., et al., 2021, The Astrophysical Journal Supplement Series, 252, 23

- Skrutskie M. F., et al., 2006, The Astronomical Journal, 131, 1163
- Soszyński I., et al., 2016, Acta Astronomica, 66, 131
- Spitzer Science C., 2009, VizieR Online Data Catalog, p. II/293
- Thompson T. A., et al., 2019, Science, 366, 637
- Traulsen I., et al., 2020, Astronomy & Astrophysics, 641, A137
- Udalski A., Szymański M., Kaluzny J., Kubiak M., Mateo M., 1992, Acta Astronomica, 42, 253
- Udalski A., Szymański M. K., Szymański G., 2015, OGLE-IV: Fourth Phase of the Optical Gravitational Lensing Experiment, <http://arxiv.org/abs/1504.05966>
- Van Etten A., Funk S., Hinton J., 2009, The Astrophysical Journal, 707, 1717
- Walter F. M., Cash W., Charles P. A., Bowyer C. S., 1980, The Astrophysical Journal, 236, 212
- Wilson R. E., Devinney E. J., 1971, The Astrophysical Journal, 166, 605
- Wolf C., et al., 2018, Publications of the Astronomical Society of Australia, 35, e010
- Wright E. L., et al., 2010, The Astronomical Journal, 140, 1868
- Zaritsky D., Harris J., Thompson I. B., Grebel E. K., Massey P., 2002, The Astronomical Journal, 123, 855
- Zaritsky D., Harris J., Thompson I. B., Grebel E. K., 2004, The Astronomical Journal, 128, 1606

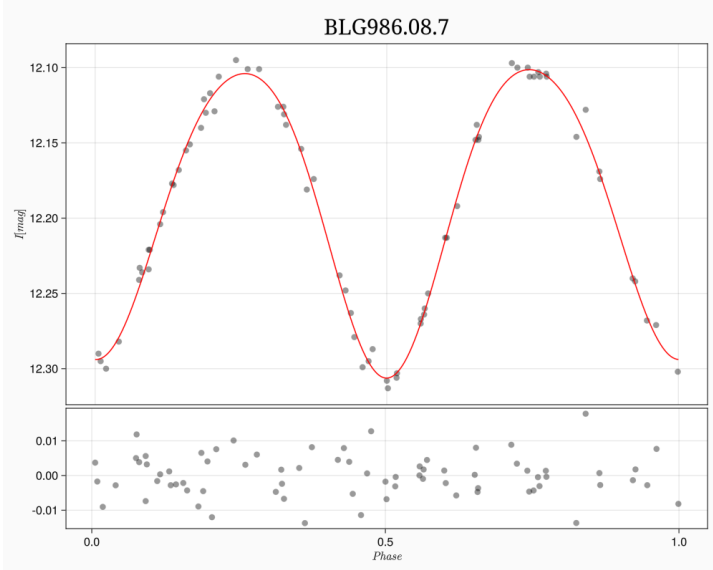
Appendices

Appendix A

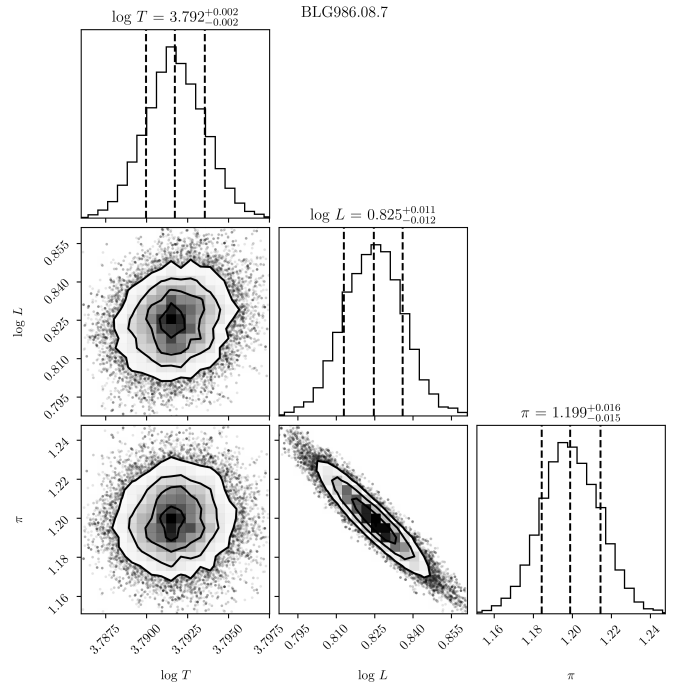
Spectral Energy Distribution plots

In the following chapter all

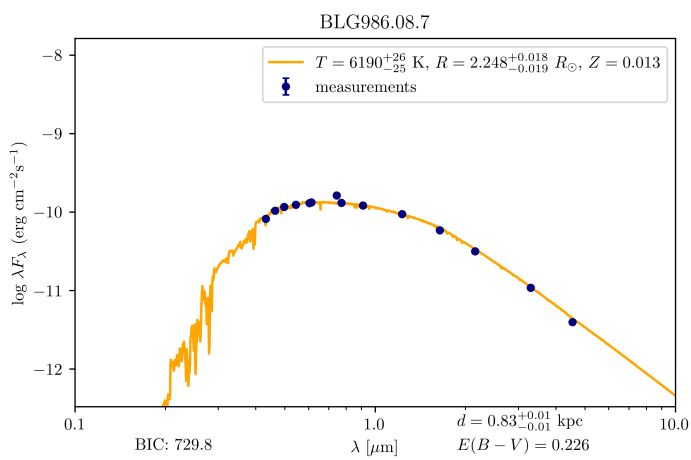
BLG986.08.7



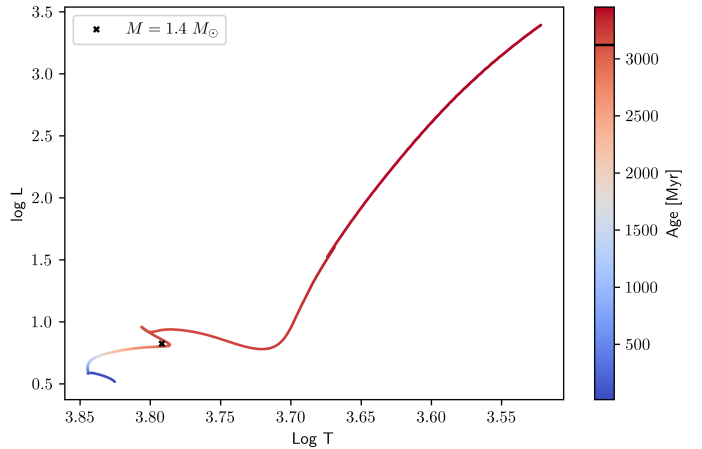
(a) Phased light curve in I mag from OGLE survey



(b) Corner plot for SED posterior estimate.

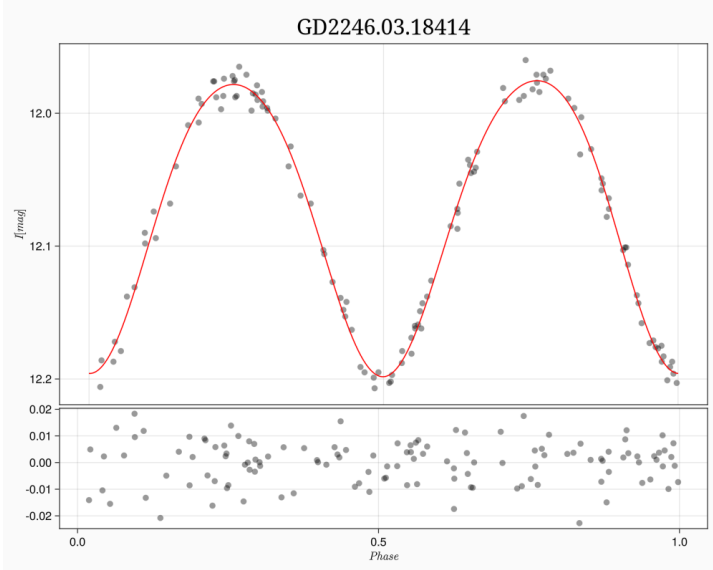


(a) Spectral Energy Distribution plot for single star model.

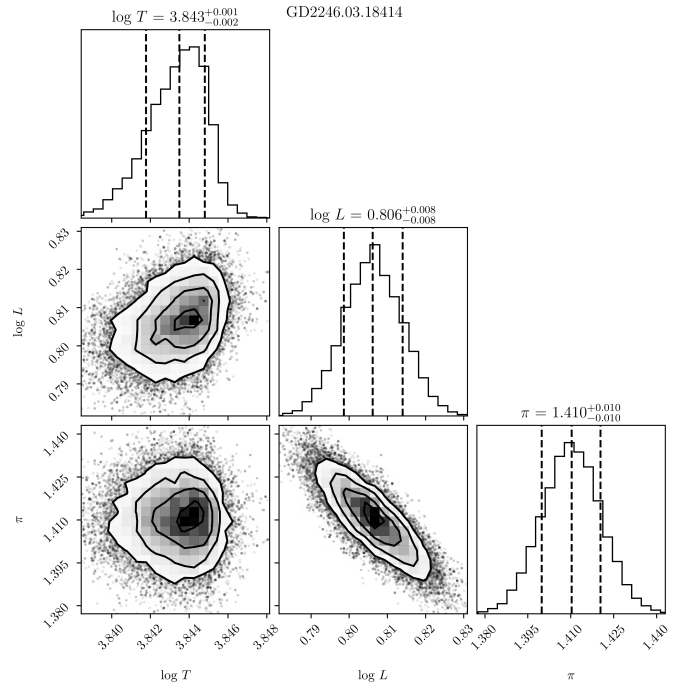


(b) Position on HR diagram together with best fitting PARSEC evolutionary track.

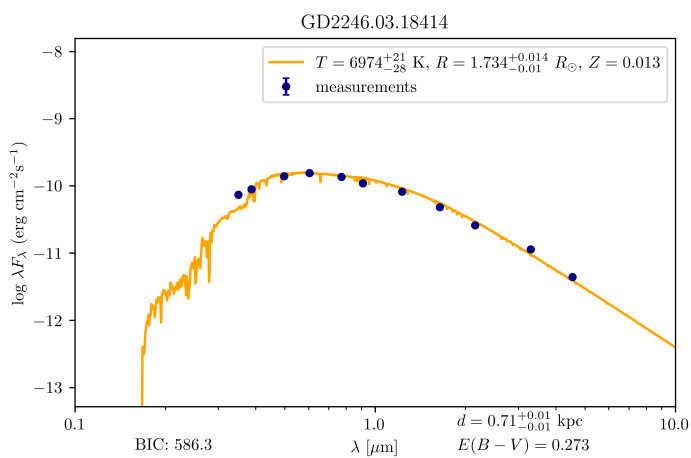
GD2246.03.18414



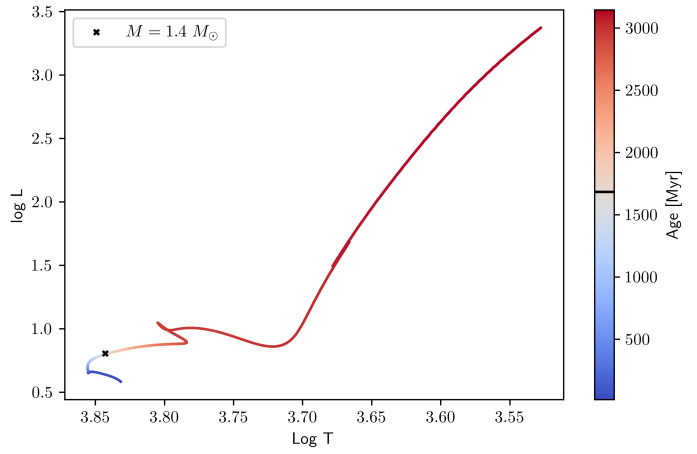
(a) Phased light curve in I mag from OGLE survey



(b) Corner plot for SED posterior estimate.

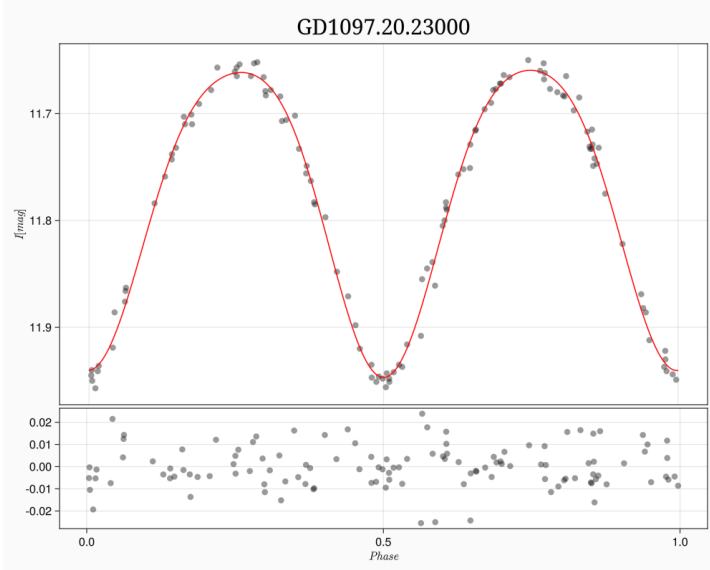


(a) Spectral Energy Distribution plot for single star model.

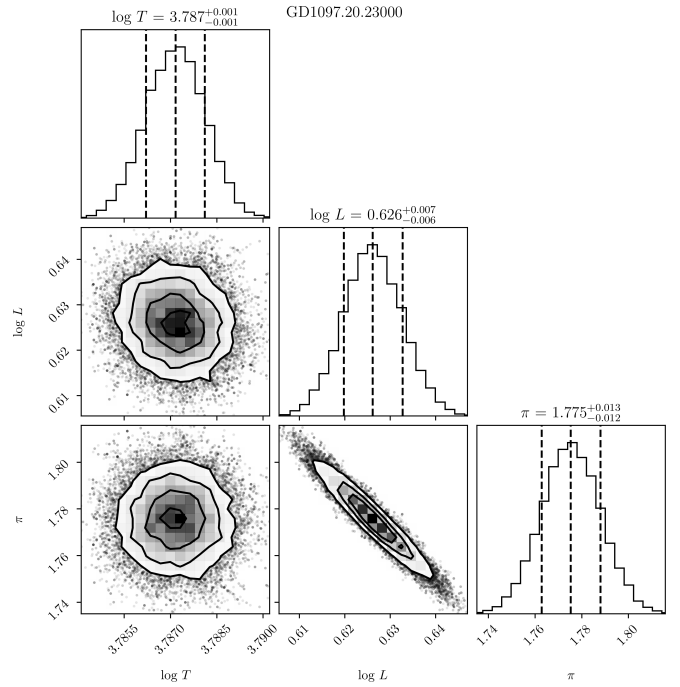


(b) Position on HR diagram together with best fitting PARSEC evolutionary track.

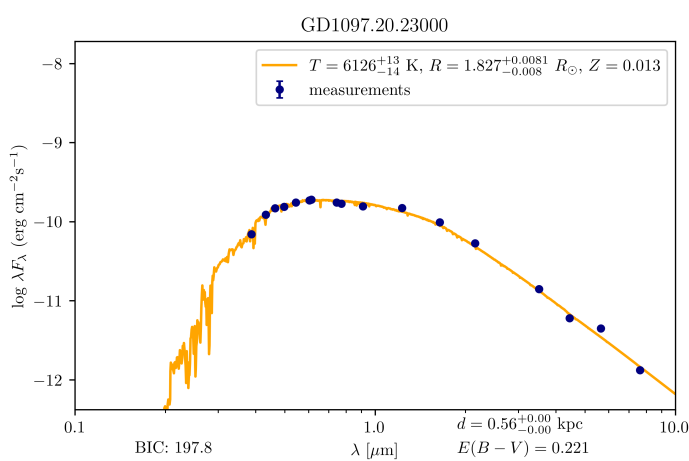
GD1097.20.23000



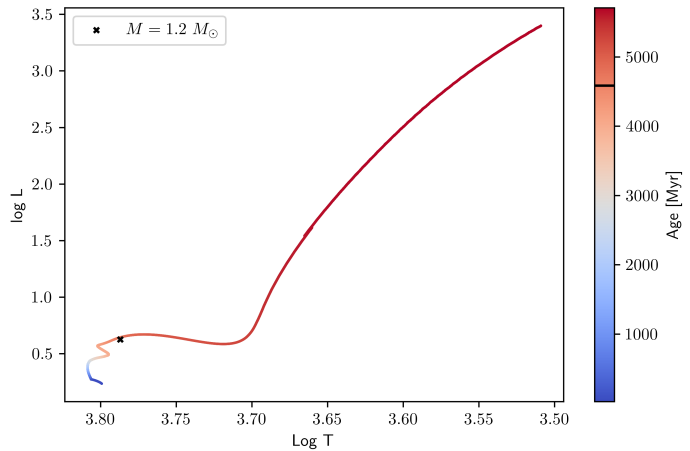
(a) Phased light curve in I mag from OGLE survey



(b) Corner plot for SED posterior estimate.

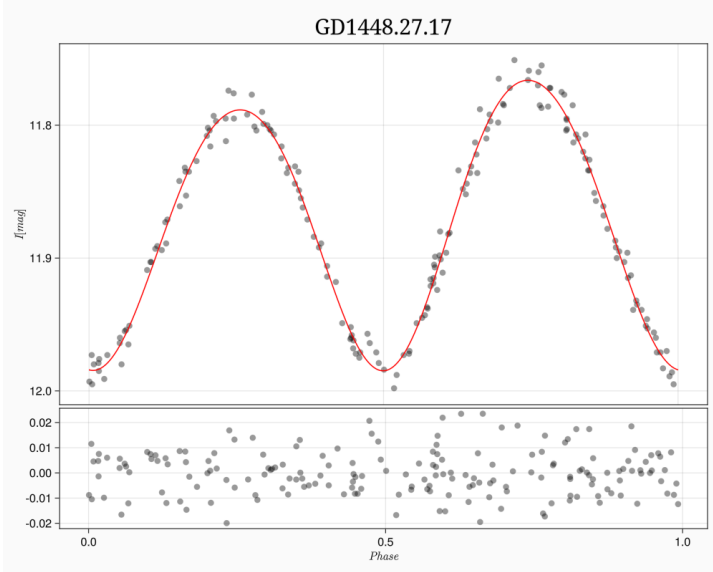


(a) Spectral Energy Distribution plot for single star model.

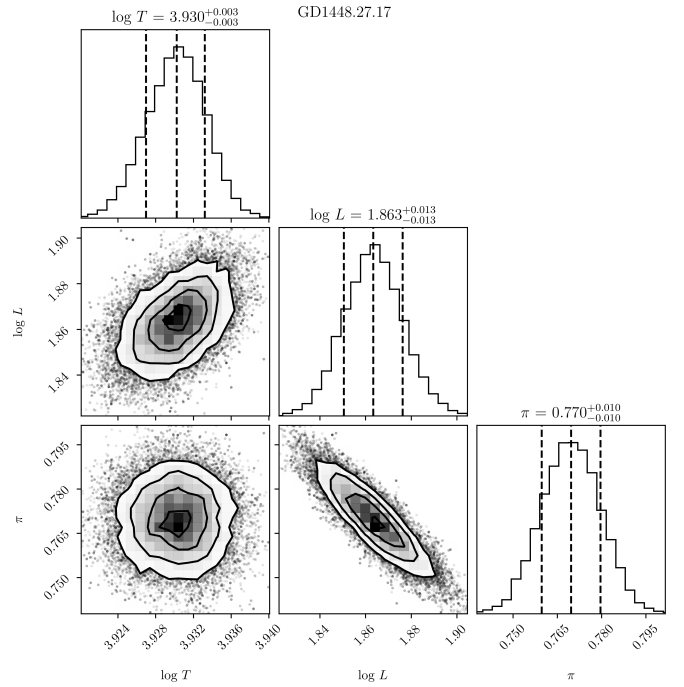


(b) Position on HR diagram together with best fitting PARSEC evolutionary track.

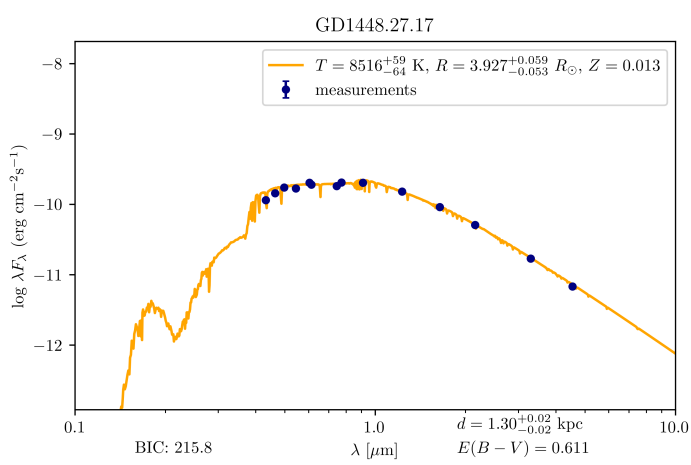
GD1448.27.17



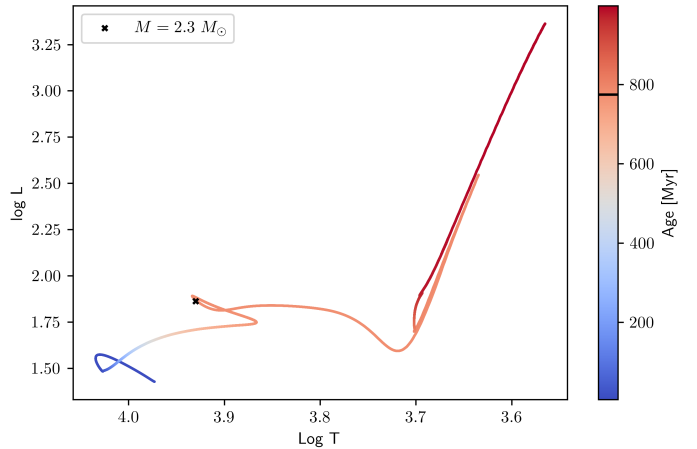
(a) Phased light curve in I mag from OGLE survey



(b) Corner plot for SED posterior estimate.

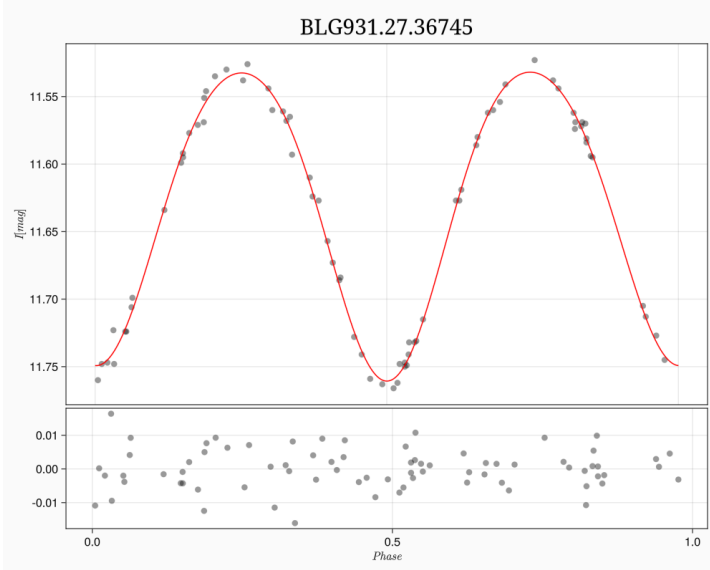


(a) Spectral Energy Distribution plot for single star model.

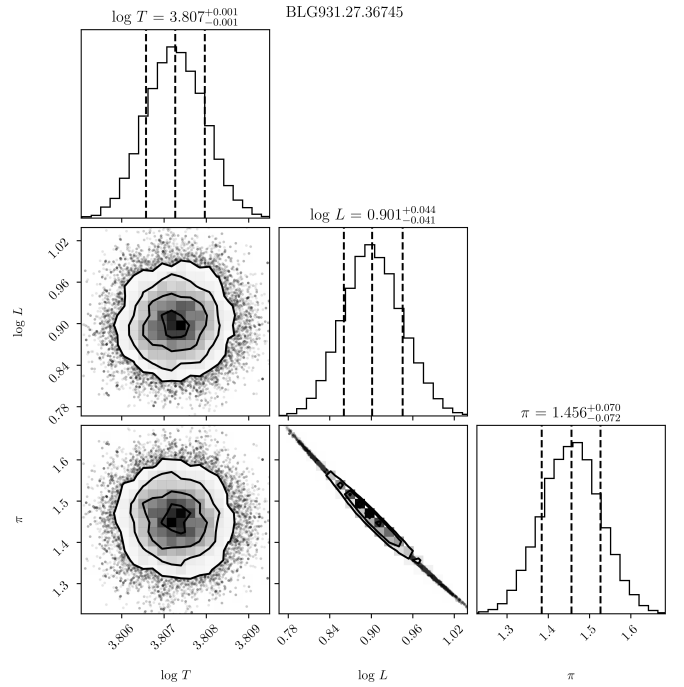


(b) Position on HR diagram together with best fitting PARSEC evolutionary track.

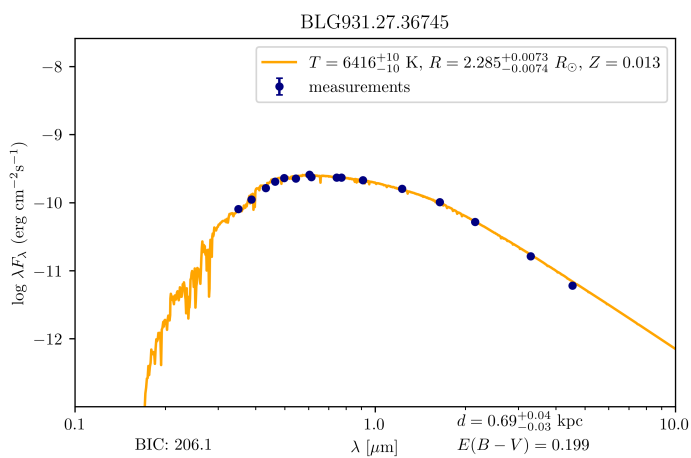
BLG931.27.36745



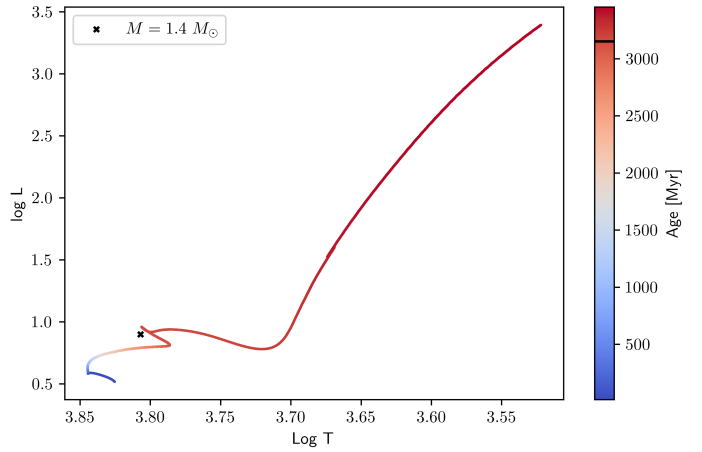
(a) Phased light curve in I mag from OGLE survey



(b) Corner plot for SED posterior estimate.

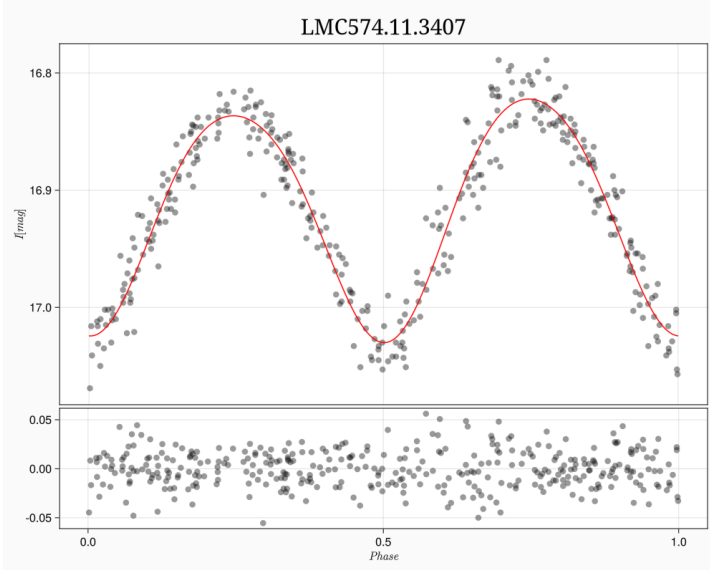


(a) Spectral Energy Distribution plot for single star model.

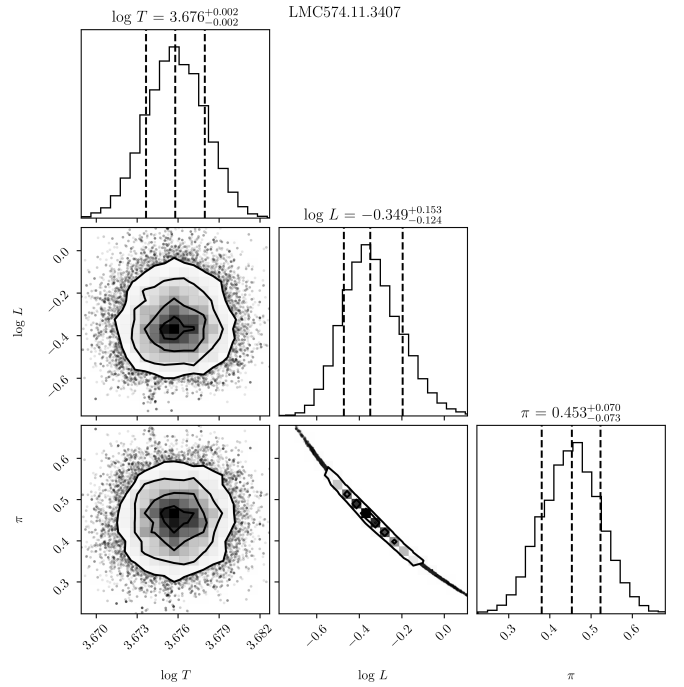


(b) Position on HR diagram together with best fitting PARSEC evolutionary track.

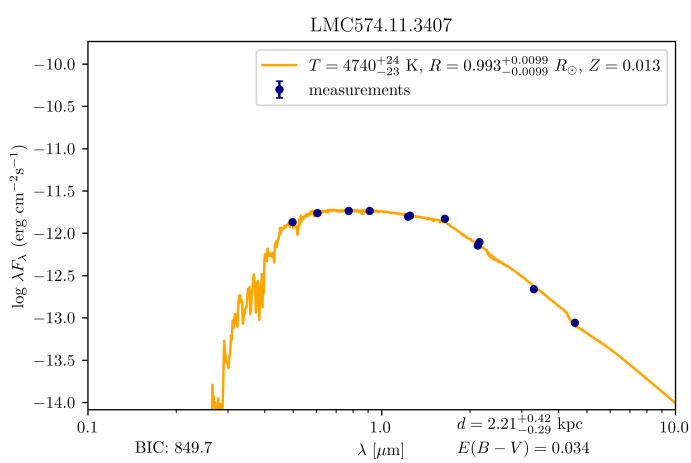
LMC574.11.3407



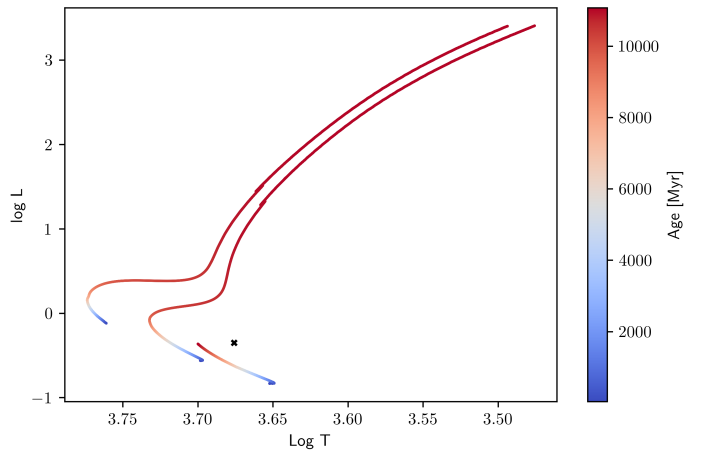
(a) Phased light curve in I mag from OGLE survey



(b) Corner plot for SED posterior estimate.

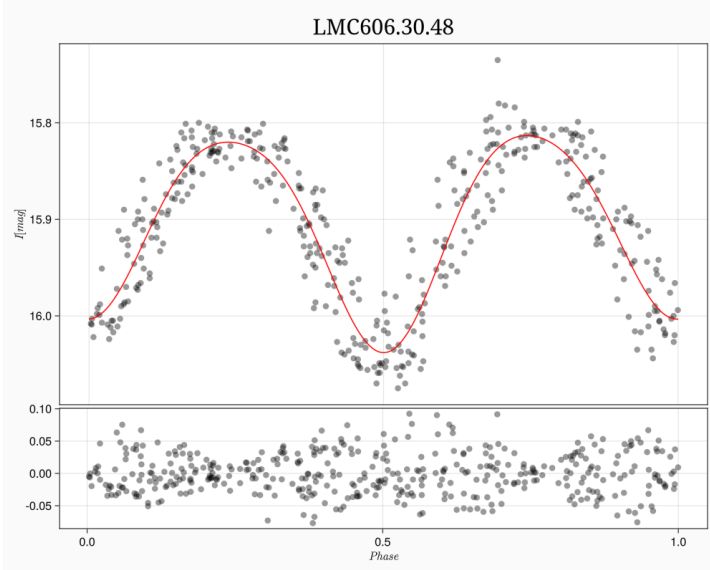


(a) Spectral Energy Distribution plot for single star model.

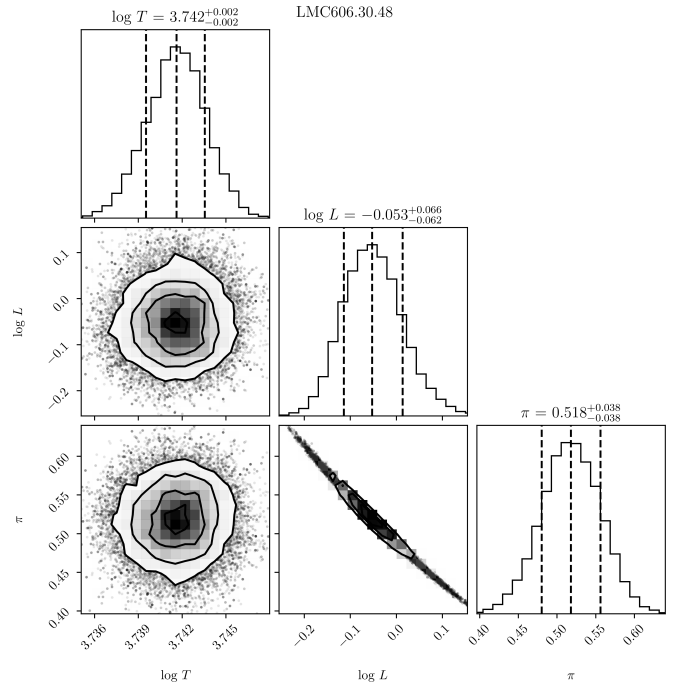


(b) Position on HR diagram together with best fitting PARSEC evolutionary track.

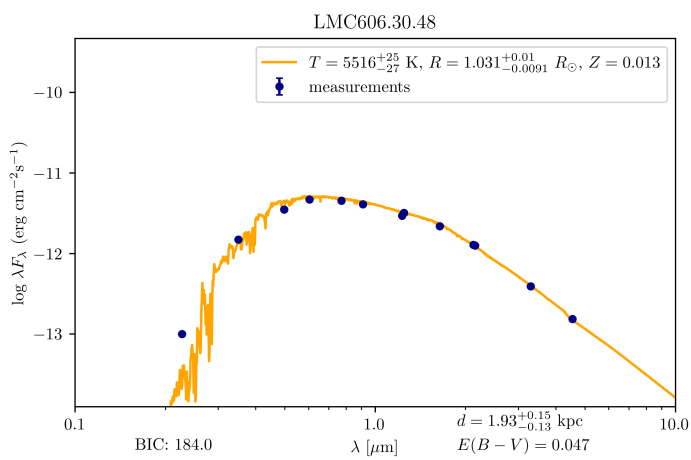
LMC606.30.48



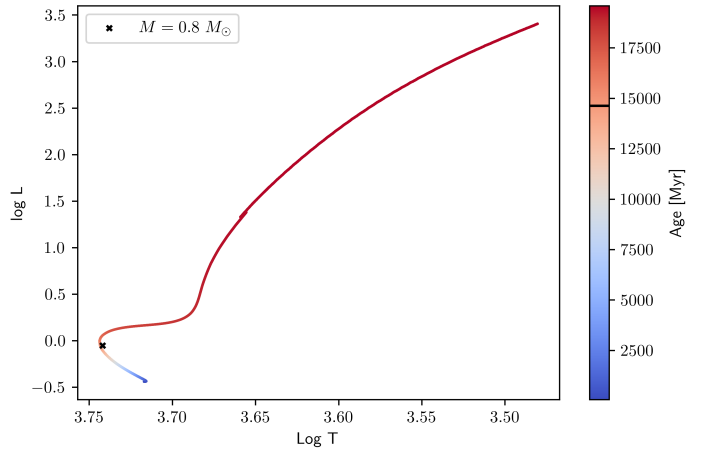
(a) Phased light curve in I mag from OGLE survey



(b) Corner plot for SED posterior estimate.

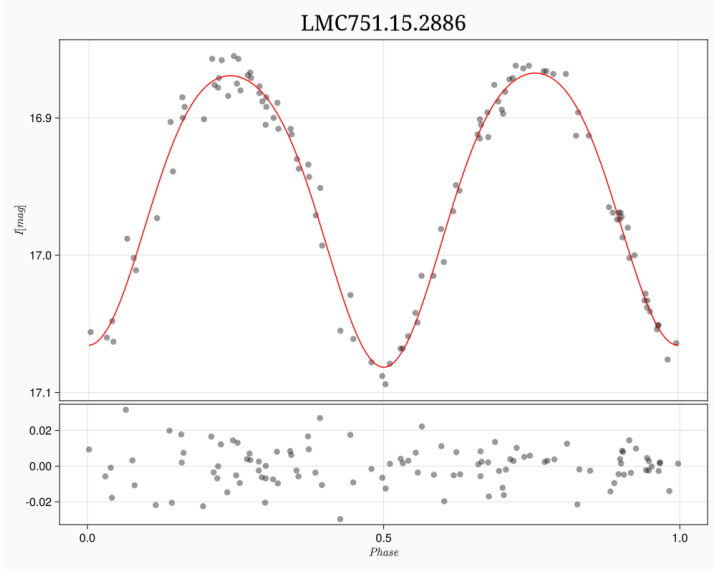


(a) Spectral Energy Distribution plot for single star model.

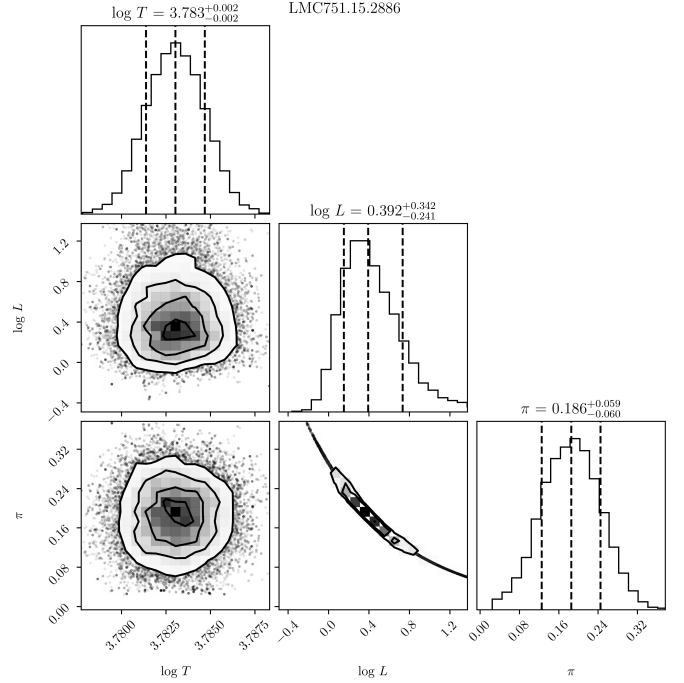


(b) Position on HR diagram together with best fitting PARSEC evolutionary track.

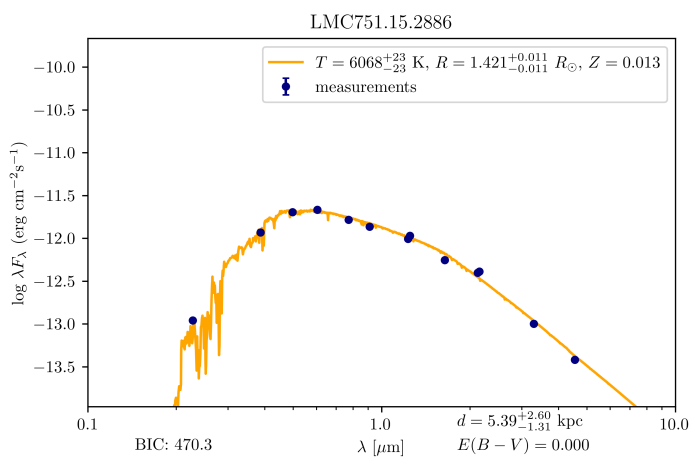
LMC751.15.2886



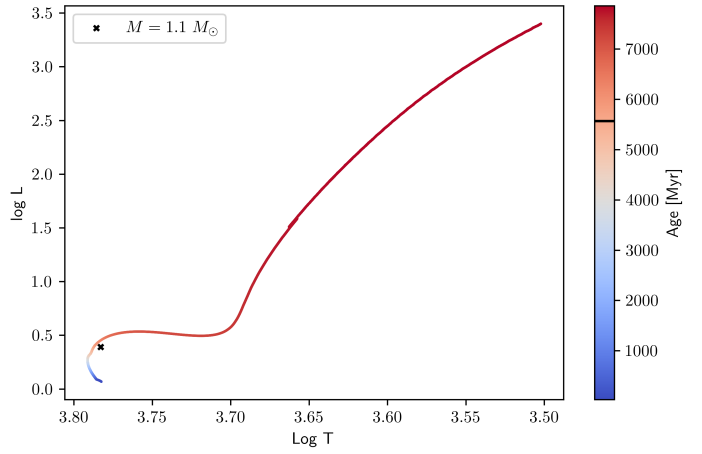
(a) Phased light curve in I mag from OGLE survey



(b) Corner plot for SED posterior estimate.

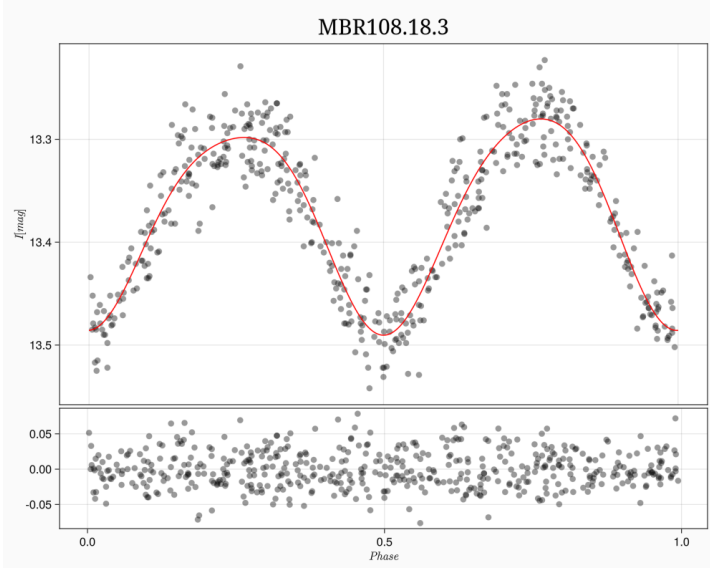


(a) Spectral Energy Distribution plot for single star model.

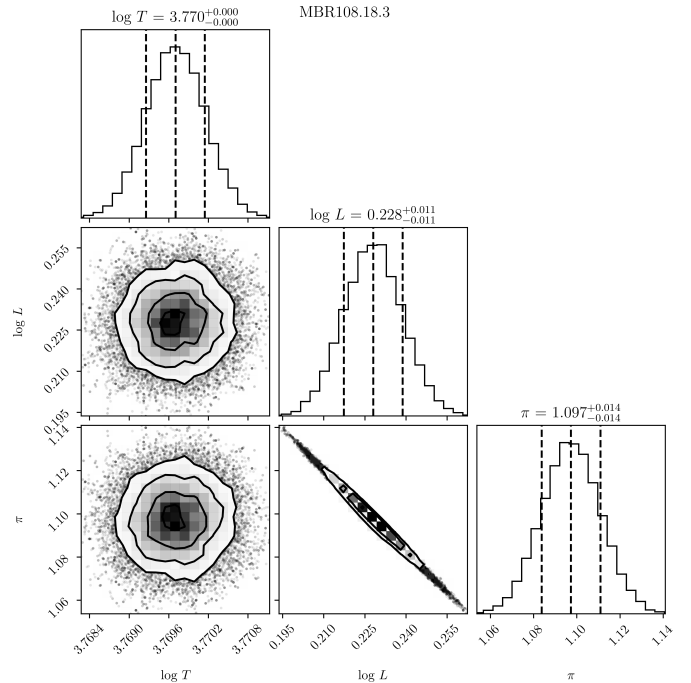


(b) Position on HR diagram together with best fitting PARSEC evolutionary track.

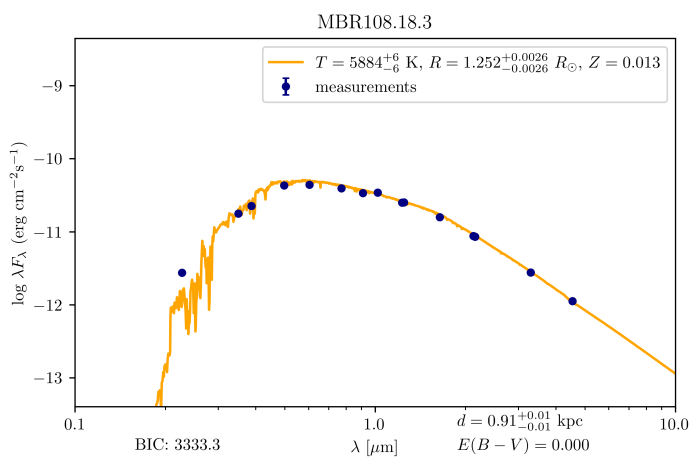
MBR108.18.3



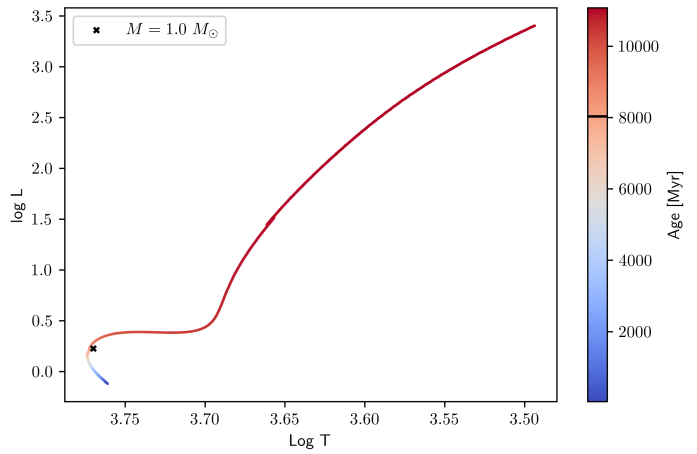
(a) Phased light curve in I mag from OGLE survey



(b) Corner plot for SED posterior estimate.

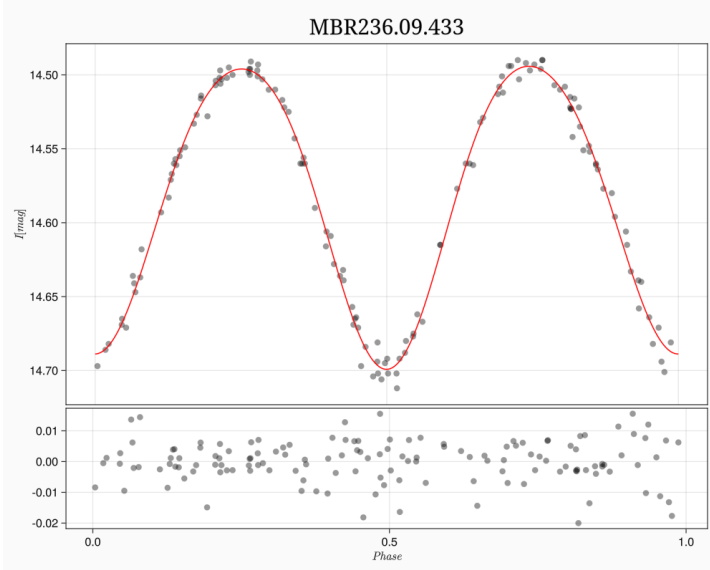


(a) Spectral Energy Distribution plot for single star model.

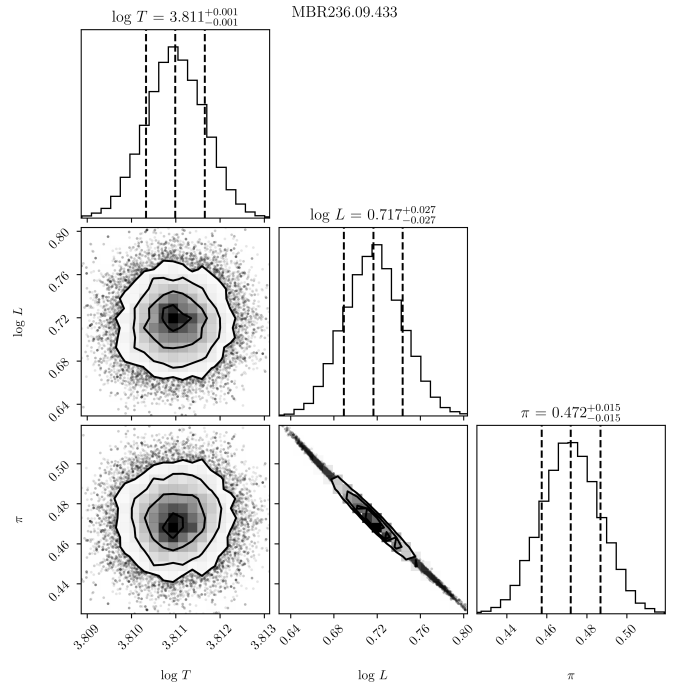


(b) Position on HR diagram together with best fitting PARSEC evolutionary track.

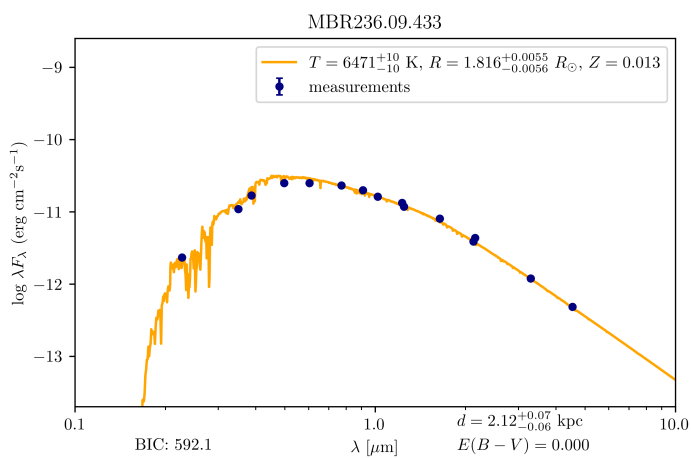
MBR236.09.433



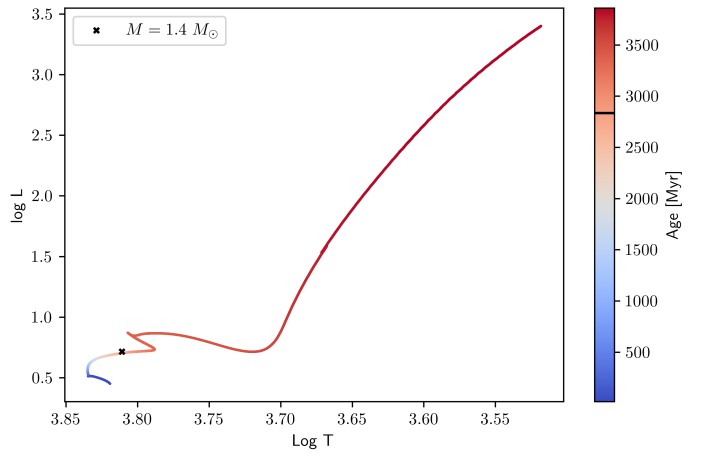
(a) Phased light curve in I mag from OGLE survey



(b) Corner plot for SED posterior estimate.

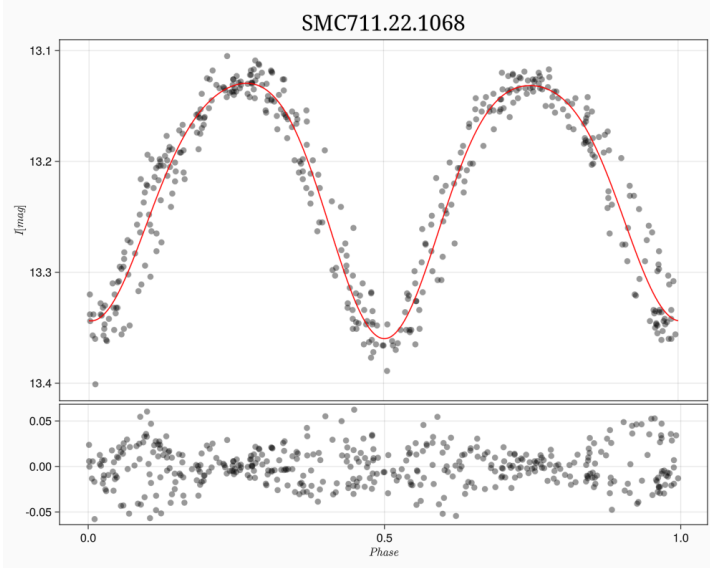


(a) Spectral Energy Distribution plot for single star model.

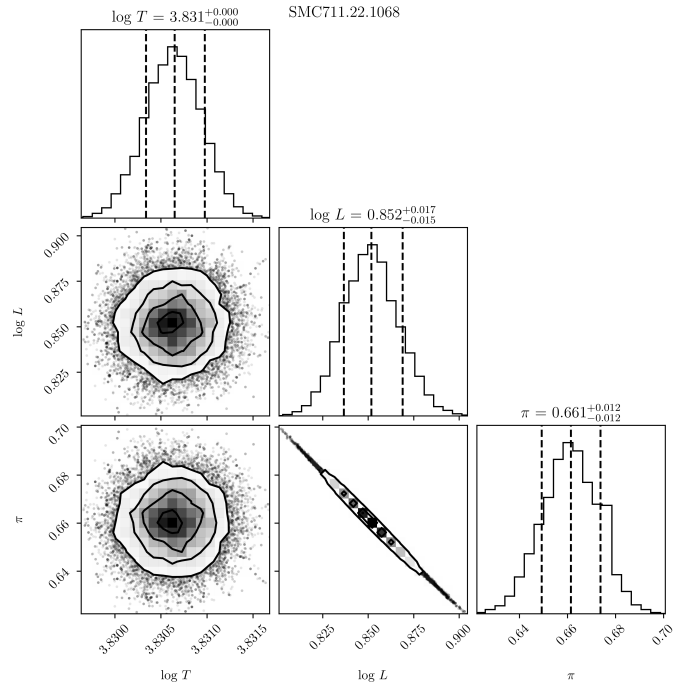


(b) Position on HR diagram together with best fitting PARSEC evolutionary track.

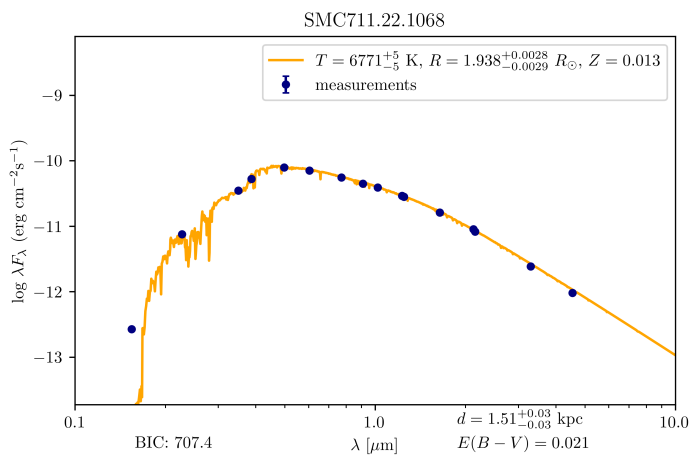
SMC711.22.1068



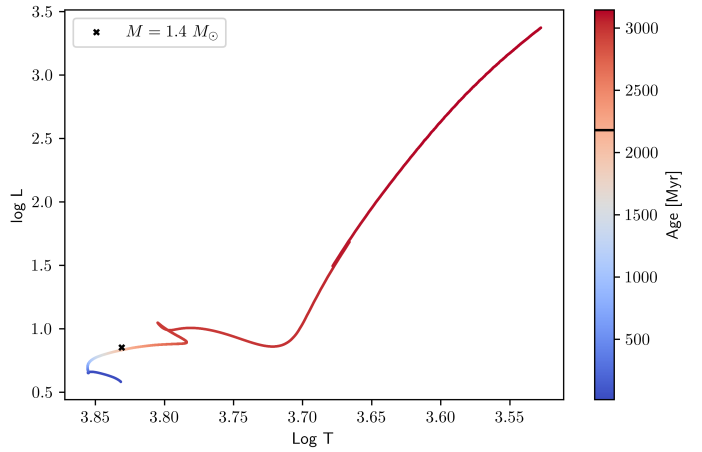
(a) Phased light curve in I mag from OGLE survey



(b) Corner plot for SED posterior estimate.

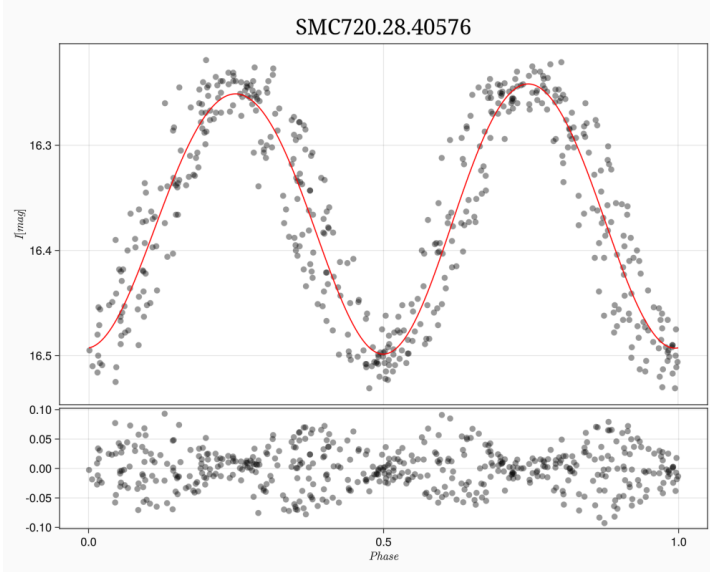


(a) Spectral Energy Distribution plot for single star model.

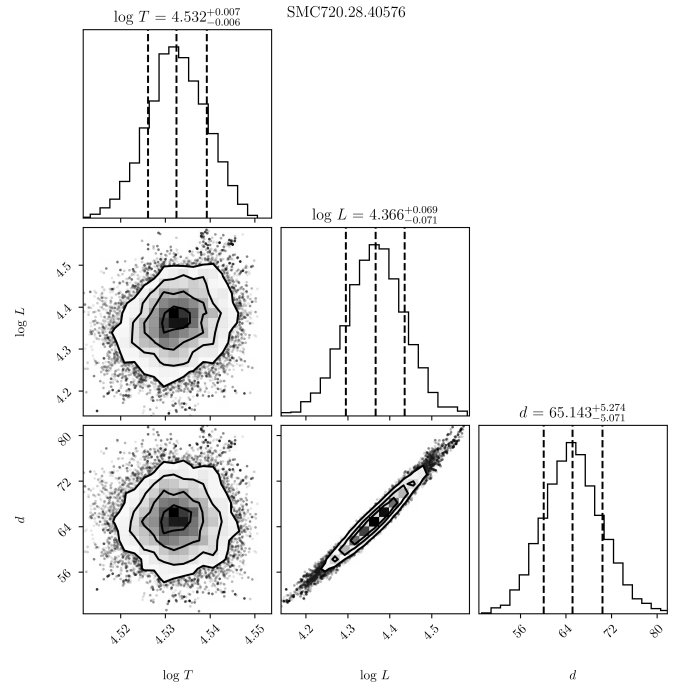


(b) Position on HR diagram together with best fitting PARSEC evolutionary track.

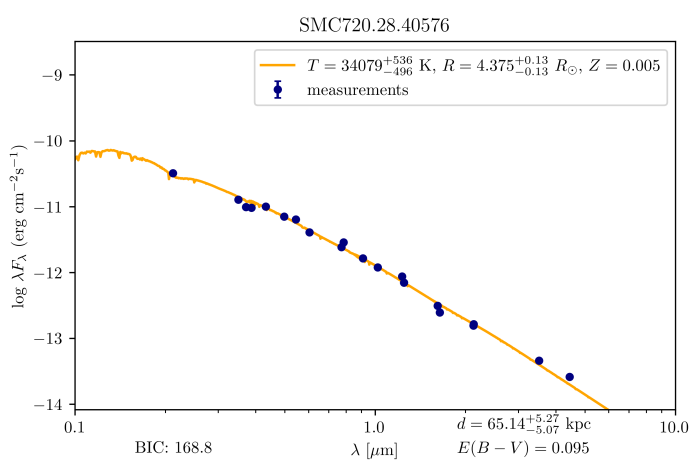
SMC720.28.40576



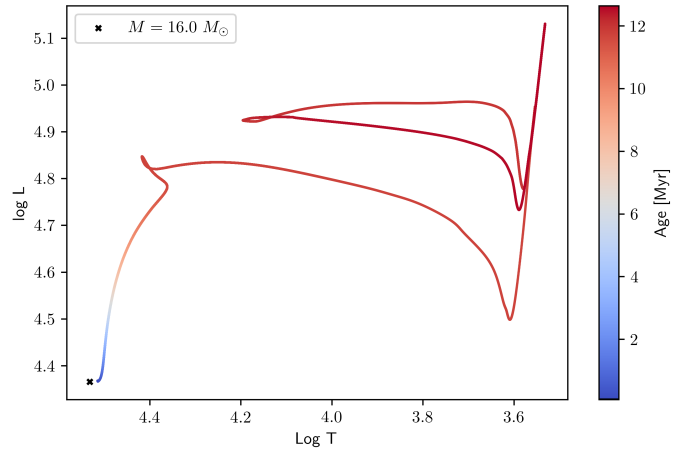
(a) Phased light curve in I mag from OGLE survey



(b) Corner plot for SED posterior estimate.

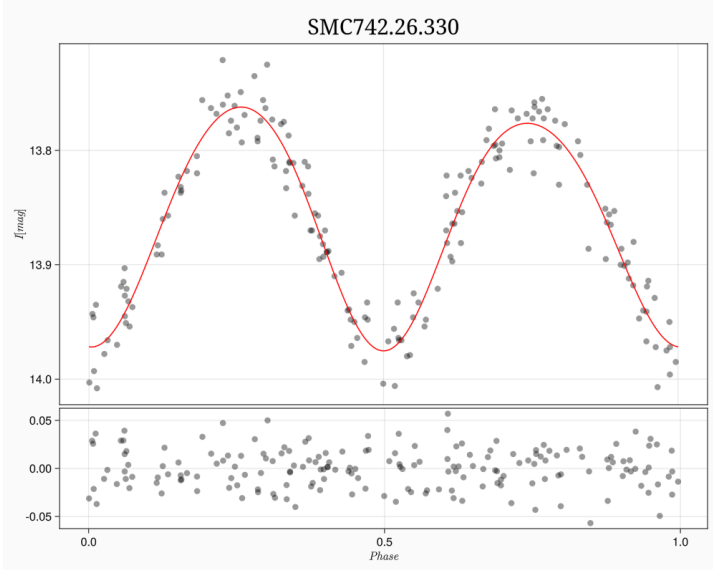


(a) Spectral Energy Distribution plot for single star model.

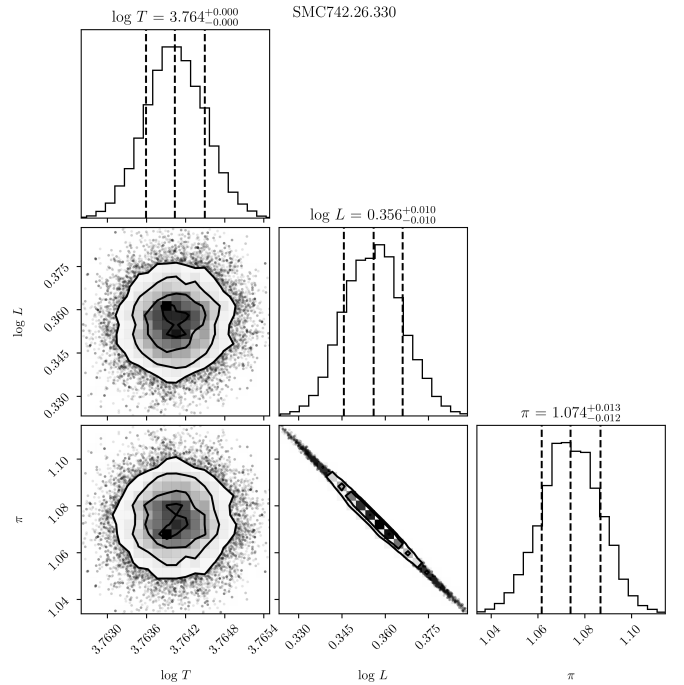


(b) Position on HR diagram together with best fitting PARSEC evolutionary track.

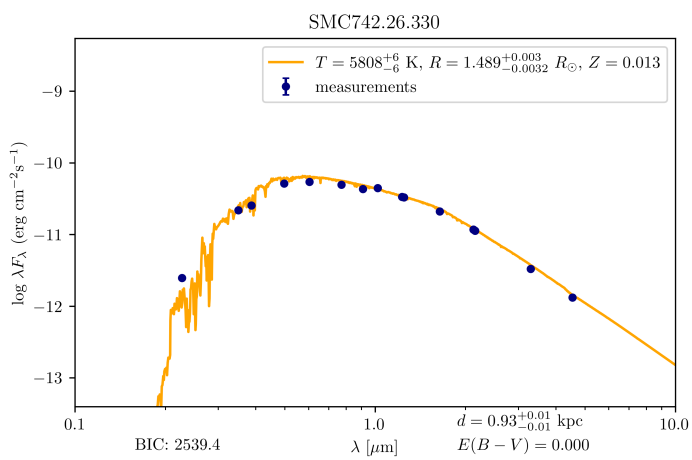
SMC742.26.330



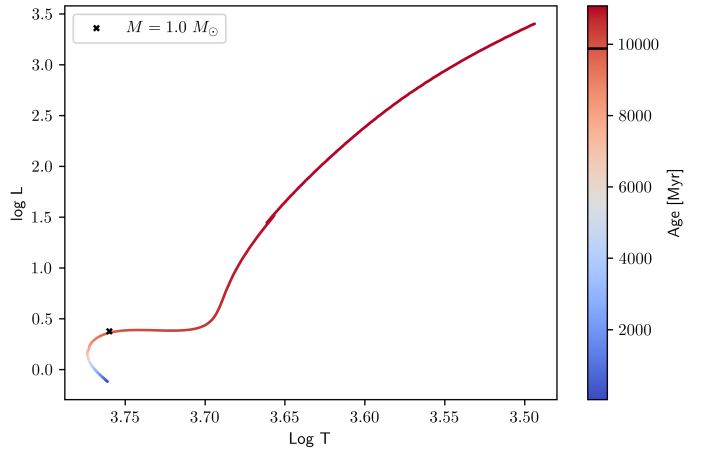
(a) Phased light curve in I mag from OGLE survey



(b) Corner plot for SED posterior estimate.



(a) Spectral Energy Distribution plot for single star model.



(b) Position on HR diagram together with best fitting PARSEC evolutionary track.

Appendix B

Semi-amplitude estimate from Gaia DR3

Let's now assume, that this radial velocity can be factored into two separate movements: center of mass movement (with velocity v_0) and circular motion with semi-amplitude K . Under following assumptions one can find, that samples of radial velocity can be written as

$$V_i = v_0 + K \cos(2\pi X_i) \quad (\text{B.1})$$

where X_i is sample from $\mathcal{U}(0, 1)$. This allows to determine, that after writing estimator of σ^2 one obtain

$$\sigma^2 = \frac{1}{n} \sum_i (\bar{V} - V_i)^2 \approx \frac{K^2}{N} \sum_i \cos^2(2\pi X_i) = \frac{K^2}{N} \sum_i \frac{\cos(4\pi X_i) + 1}{2} \quad (\text{B.2})$$

where simplification $\bar{V} \approx v_0$ is used. Now one would like to obtain some statistical properties of this variance estimator such as expected value and variance. It can be clearly seen that $\mathbb{E} \cos(4\pi X_i) = 0$ while $\widehat{\text{Var}}(\cos 4\pi X_i) = \frac{1}{8}$. While first value is straightforward as mean of cosine is equal to zero second one is more complicated but follows from the fact that $\cos(4\pi X_i)$ is arcsine distributed and it's variance it's well known. Hence

$$\mathbb{E}\sigma^2 = \frac{K^2}{2N} \cdot N = \frac{K^2}{2} \quad (\text{B.3})$$

$$\widehat{\text{Var}}(\sigma^2) = \frac{K^4}{32N^2} \cdot N = \frac{K^4}{32N} \quad (\text{B.4})$$

Those two values allow us to determine quality of estimator, using Central Limit Theory one can also approximate that

$$\sigma^2 \sim \mathcal{N}\left(\frac{K^2}{2}, \frac{K^4}{32N}\right) \quad (\text{B.5})$$

which can be quite useful to estimate K from obtained data (for most of the objects $N > 17$ so Central Limit Theorem gives good approximation). There are many simplification

made here which are mainly based on the fact it's not entirely known how Gaia obtains RV measurements and what is measured after all. If one assumes that true velocity is contaminated by gaussian noise with standard deviation σ_{noise} estimated variance will be shifted and

$$\mathbb{E}\sigma^2 = \frac{K^2}{2} + \sigma_{noise}^2 \quad (\text{B.6})$$

so K will be overestimated.